



Investigating the significance of flatness defects in the origin of hysteresis in flag flutter

Holger Mettelsiefen¹, Sunetra Sarkar²  and Vrishank Raghav¹ 

¹Department of Aerospace Engineering, Auburn University, Auburn, AL 36849, USA

²Department of Aerospace Engineering, Indian Institute of Technology Madras, Chennai 600036, Tamil Nadu, India

Corresponding author: Vrishank Raghav, raghav@auburn.edu

(Received 13 December 2024; revised 30 July 2025; accepted 1 September 2025)

Flag flutter frequently features a marked difference between the onset speed of flutter and the speed below which flutter stops. The hysteresis tends to be especially large in experiments as opposed to simulations. This phenomenon has been ascribed to inherent imperfections of flatness in experimental samples, which are thought to inhibit the onset of flutter but have a lesser effect once a flag is already fluttering. In this work, we present an experimental confirmation for this explanation through motion tracking. We also visualize the wake to assess the potential contribution of discrete vortex shedding to hysteresis. We then mould our understanding of the mechanism of bistability and additional observations on flag flutter into a novel, observation-based, semiempirical model for flag flutter in the form of a single ordinary differential equation. Despite its simplicity, the model successfully reproduces key features of the physical system such as bistability, sudden transitions between non-fluttering and fluttering states, amplitude growth and frequency growth.

Key words: low-dimensional models, flow-structure interactions, bifurcation

1. Introduction

When the motion of a solid body and the flow of a fluid around the body cannot be understood or computed independently, the combined mechanical system must be treated as a case of fluid–structure interaction (FSI). In FSI problems, the structural motion and the flow field evolve together, being coupled by the fluid forces that act at the surface of the solid and by the solid’s displacements.

One category of FSI problems deals with the motion of typically flat, rectangular, thin and often inextensible structures in a steady flow. Generally, the flow aligns with the plane

of the structure's neutral shape and impinges perpendicular to one edge. The leading edge is usually either pinned or most commonly clamped, known as conventional flag flutter. Conversely, clamping the trailing edge results in an inverted flag, which is promising for energy harvesting (Shoele & Mittal 2016). Other configurations include plates clamped normally to one wall of a flow channel (Lee *et al.* 2017), plates fixed at a lateral edge (Dou *et al.* 2020) or various other permutations of boundary conditions (Mavroyiakoumou & Alben 2022). When the bending stiffness is negligible, it is referred to as membrane flutter and when high, it is plate flutter. According to Yu, Liu & Amandolese (2019), we use the term flag, given our moderate bending stiffness. We consider the flag clamped at the leading edge, fixing all translational and rotational freedoms there.

Conventional flag flutter has been studied both as a canonical problem of FSI (Thoma 1939) and in contexts such as snoring (Huang 1995; Howell *et al.* 2009), high-speed printing (Watanabe *et al.* 2002), energy harvesting (Allen & Smits 2001; Michelin & Doaré 2013; Özkan *et al.* 2024), flow sensing (Liu *et al.* 2012), heat transfer (Shoele & Mittal 2014) and bioinspired propulsion (Müller 2003; Shelley, Vandenberghe & Zhang 2005; Kim, Huang & Sung 2010). Some studies of leaflet flutter in bioprosthetic heart valves have also referred to flag flutter (Avelar *et al.* 2017; Johnson *et al.* 2020). Researchers have employed water and air experiments, linear and nonlinear stability analysis and two-dimensional/three-dimensional simulations with varying degrees of fidelity. Comprehensive reviews can be found in Shelley & Zhang (2011), Gallegos & Sharma (2017) and Yu *et al.* (2019). We first discuss conventional flag flutter physics before addressing bistability and the objectives of this paper.

1.1. Background

In conventional flag flutter, a destabilizing pressure field arises from opposing pressures across the flag when it undergoes wavy deformation (Thoma 1939), while viscous drag induces tension (Connell & Yue 2007), and the flag's bending stiffness and structural damping counteract deflection (Eloy, Kofman & Schouveiler 2012). At low flow speeds, the flag remains straight but transitions to a large-amplitude limit cycle oscillation (LCO) as the flow speed exceeds the critical value, U_c , a phenomenon referred to as flutter. Intermediate states can occur, such as random vibrations with tip movements far smaller than the flag's length, potentially due to turbulence or mounting-induced vibrations, or small-amplitude LCOs that appear prior to flutter, as noted by Tang, Yamamoto & Dowell (2003). Sufficient structural inertia is required for flutter, and the fluid's added mass alone cannot induce flutter in a massless flag (Zhu & Peskin 2002; Tian 2013).

Assuming an isotropic solid material and neglecting both structural damping and gravity, the governing dimensionless parameters (Connell & Yue 2007; Eloy *et al.* 2012) are

$$\underbrace{\mu \equiv \frac{m}{\rho_f L}}_{\text{Mass ratio}}, \quad \underbrace{U^* \equiv UL \sqrt{\frac{m}{D}}}_{\text{Reduced velocity}}, \quad \underbrace{Re_L \equiv \frac{UL}{\nu_f}}_{\text{Reynolds number}}, \quad \underbrace{H^* \equiv \frac{H}{L}}_{\text{Aspect ratio}}, \quad \underbrace{\frac{H}{h}}_{\text{Thickness ratio}}, \quad (1.1)$$

where $m \equiv \rho_s h$ with ρ_s the structural mass density and h the thickness, ρ_f is the fluid density, L the length, U the flow speed, $D = Eh^3/(12(1 - \nu^2))$ the plate bending stiffness with E the elastic modulus and ν Poisson's ratio, ν_f the fluid's kinematic viscosity, H the height or equivalently the width of the flag (refer to figure 1 for orientation). The ratio of height to thickness, H/h , is rarely addressed in the literature since h is often not explicitly considered a geometric parameter, typically appearing only within m and D . We include H/h here because it affects the flag's bending stiffness sensitivity to transverse flatness

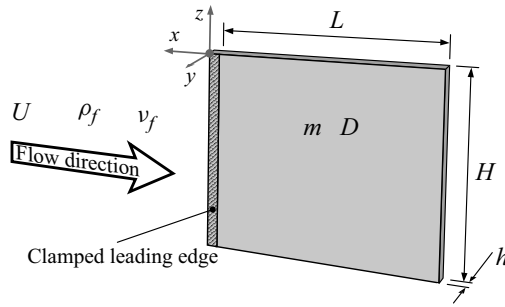


Figure 1. Illustration of a conventional flag in axial flow with the relevant physical quantities: fluid velocity U ; density ρ_f ; kinematic viscosity ν_f ; flag length L ; height H ; thickness h ; area-specific mass m ; plate bending stiffness D .

defects, a topic further explored in § 1.3. The critical reduced velocity at flutter onset, U_c^* , depends on μ , Re_L and H^* . In cases of minimal bending stiffness, viscous drag-induced tension dominates the restoring force, and the critical speed may rather be expressed in terms of Re_L , as in Connell & Yue (2007). Conversely, if viscous drag is minor with respect to bending forces, the Reynolds number loses significance. This work examines finite bending stiffness with Reynolds numbers that cannot be considered low (see § 2.6).

The initial flutter mode shape of a flag is determined by the mass ratio, μ (Tang & Paidoussis 2007). The simplest mode resembles the second eigenmode of a cantilevered beam, while for $\mu \lesssim 0.66$, higher modes appear (Eloy *et al.* 2008; Michelin, Smith & Glover 2008). The motion resembles a beam bending mode but always includes a component of a wave moving downstream (Langthjem 2019). Without bending stiffness, a purely downstream travelling wave is seen; with finite stiffness, wave reflections at the free tip create a partially standing wave (Moretti 2004). Michelin *et al.* (2008) observed that while the kinematics is dominated by downstream wave motion, pressure waves travel upstream from the trailing edge. With growing flow speed, the flag can transition to modes with more necks (or pseudonodes) (Viro, Amandolese & Hémon 2013). At high speeds, motion becomes chaotic, with intense tip snapping (Connell & Yue 2007; Viro *et al.* 2013). This paper excludes such regimes, and ‘flutter’ herein denotes periodic motion only.

The frequency of flutter, f , is proportional to flow speed with $Str_L \equiv fL/U$ of the order of 0.23 in one-neck flutter (Yu *et al.* 2019), whereas the amplitude, A , saturates at some flow speed and can decrease slightly thereafter (Eloy *et al.* 2012). The amplitude-based Strouhal number, Str_A , expressed as $2fA/U$ per Connell & Yue (2007), remains roughly constant with saturated amplitude. Reducing μ from a high value (e.g. $\mu = 10$ for one-neck flutter) raises the flow speed needed for flutter (U_c) (Michelin *et al.* 2008). Conversely, increasing flag mass while maintaining stiffness lowers the flow speed required for flutter. At lower μ , as higher flutter modes emerge, the amplitude of periodic motion is less than at larger μ (Alben 2022).

The nature of the coupling between fluid and solid motion in conventional flag flutter is understood through the relevant time scales. The parameter U^* represents the ratio between the time scale of a freely vibrating plate, $\sqrt{mL^4/D}$, and the fluid convection time scale, L/U (Tang & Paidoussis 2007). For a specific vibration mode, a constant factor affects the plate vibration time scale. For example, the second mode of a cantilevered plate has an angular frequency $\omega = 4.694^2 \sqrt{D/(mL^4)}$ (adapted from Han, Benaroya & Wei (1999)), with motion between extrema taking $\pi/\omega = 0.14 \sqrt{mL^4/D}$. In experiments with high Reynolds numbers and mass ratios typical for wind or water tunnel experiments,

U_c^* is around 10 (Michelin *et al.* 2008). Including the 0.14 factor in the plate motion time scale indicates that the time scales are comparable. The approximate value $Str_A \approx 0.2$ for large-amplitude flutter (Yu *et al.* 2019) reinforces this, as harmonic motion at frequency f reaches maximum velocity $2\pi f A$, with $2\pi f A/U = \pi Str_A \approx 0.63$. If inertia is adequate, L and $2A$ are comparable, showing similar time scales for flow and flag motion. This implies significant roles for added mass, damping and stiffness in dynamics, suggesting ‘strong coupling’ (Viot *et al.* 2013).

1.2. Bistability and hysteresis

The onset and termination of flutter with changes in U are significant to both exploit and avoid flutter phenomena. Numerous studies seek to predict the critical onset speed, U_c , at which a flag begins fluttering. Interestingly, flags can have a velocity range, (U_d, U_c) , where both stationary and fluttering states are stable, with U_d being the speed where flutter stops. This bistability leads to hysteresis of the motion state with varying flow speed. We define hysteresis extent as $\mathcal{E} \equiv (U_c - U_d)/U_d$, where U_d is the baseline and U_c an augmentation of U_d . The literature and our findings show that in experiments, \mathcal{E} often reaches two-digit percentage range, such as 28 % reported by Eloy *et al.* (2008). Conversely, in mathematical models, bistability is reduced or absent, with experimental U_d aligning more closely with stability analysis than experimental U_c (Eloy *et al.* 2008, 2012). Only models incorporating nonlinear fluid dynamics exhibit bistability (Zhu & Peskin 2002; Connell & Yue 2007; Alben & Shelley 2008; Michelin *et al.* 2008; Hiroaki & Watanabe 2024), contrary to linear fluid models (Tang *et al.* 2003).

Fluid nonlinearity in flag flutter is notably influenced by the wake, as modelled in all five studies referenced above. In instances of large-amplitude flutter, the wake exhibits organized vortex streets, similar to observations by Connell & Yue (2007) and Giacomello & Porfiri (2011). These vortices provide pressure feedback affecting system dynamics (Alben & Shelley 2008), potentially amplifying flutter (Martin 2006). Including the vortical wake in stability analyses shows a destabilizing impact, lowering critical speed (Langthjem 2019). We speculate that the vortical wake may sustain motion for some conditions within $U_d < U < U_c$. Interestingly, Tang & Païdoussis (2007) did not observe hysteresis in their linear aerodynamic model, but introduced it by altering the wake artificially. Conversely, Hiroaki & Watanabe (2024) found some hysteresis even without vortex shedding in their nonlinear model, suggesting minimal wake influence on hysteresis.

Boundary layer separation, integral to nonlinear fluid phenomena like dynamic stall, likely has minimal impact on hysteresis. During flag flutter, the boundary layer can remain fully attached, as indicated by Gibbs *et al.* (2014) and Jia *et al.* (2018). In simulations assuming negligible bending stiffness, Connell & Yue (2007) demonstrated flow fields lacking separation on the flag or exhibiting only minor separation bubbles during irregular flutter (their figure 9). While nonlinear fluid dynamics may induce hysteresis, the highest \mathcal{E} observed in numerical studies was only 5.2 % (Michelin *et al.* 2008). Consequently, factors apart from nonlinear fluid dynamics must account for the large hysteresis noted in experiments.

1.3. Hypotheses and aims of this study

Several hypotheses on the discrepancies between models and experiments have been proposed, see Tang & Païdoussis (2007) for example. Building on the hypotheses of Tang & Païdoussis (2007) and Eloy *et al.* (2008), Eloy *et al.* (2012) experimentally showed that adding a minor transverse curvature increases the onset speed of a plastic flag while

leaving the stop speed largely unchanged. This was attributed to the stiffening effect of the curvature, assuming that Gaussian curvature has a prohibitively high energetic cost. That is, transverse flatness defects restrict motion until suppressed by large-scale longitudinal bending at a critical onset speed and remain suppressed until the speed falls below a critical stop speed. They proposed that such defects become significant when their magnitude is comparable to or exceeds the flag's thickness, which can happen in practice even without intentional introduction of such defects, and that larger aspect ratios H^* exacerbate this effect. In support of this, the literature on plate mechanics shows that the stiffening of a rectangular plate by constant longitudinal and transverse curvatures, κ_x and κ_y , scales with $H^{*2}(H/h)^2(\kappa_y - \nu\kappa_x)^2$, based on Pini *et al.* (2016). A transverse flatness defect is represented by $H\kappa_y$, whose ratio with h appears squared in this scaling law when $\kappa_x = 0$. The dependency on H^{*2} indicates that slender flags are less susceptible than wide ones.

This study examines flatness defects, which appear to account for most of the hysteresis noted in experiments (Eloy *et al.* 2012). Due to the lack of surface motion tracking in existing flag flutter research, the primary objective here is to provide direct experimental evidence for the explanation proposed by Eloy *et al.* (2012) using high-resolution stereophotogrammetry. We will analyse surface shape variations during a velocity sweep to understand how small-scale flatness defects evolve along with large-scale motion. In addition, motion tracking data will be examined to illustrate the mechanism of flag flutter. Moreover, flow visualization will be used to qualitatively evaluate the wake structure for discussing the significance of discrete vortex shedding in hysteresis.

To our knowledge, all current models for flag flutter are defined in continuous space with many degrees of freedom, such as two-way coupled computational fluid mechanics–finite element method models (Connell & Yue 2007), vortex sheet models (Alben & Shelley 2008) and discrete vortex models (Michelin *et al.* 2008), or those for analytical stability analysis (Connell & Yue 2007). Despite the existence of low-dimensional models based on as few as two ordinary differential equations (ODEs) for other canonical FSI problems like vortex-induced vibrations (VIVs) (Facchinetti *et al.* 2004), no such model is available for flag flutter. Employing phenomenological low-order ODE models can aid in understanding the physics involved, though they may not represent all aspects of the system. Thus, the secondary aim of this paper is to introduce and evaluate an observation-based semiempirical model that employs a single ODE to capture several characteristics of flag flutter. The model is constructed from first principles rather than by linearizing the complete set of partial differential equations, which would limit its capacity to capture jump-nonlinearities. Bistability is incorporated via a nonlinear stiffness term, inspired by the explanation of Eloy *et al.* (2012) and our experimental findings. Unlike existing models, our model can be configured to feature large hysteresis.

2. Experimental methods

Here we describe how we obtained critical flow speeds and high-resolution motion tracking data of fluttering flags. Edge tracking was done to obtain tip motion amplitudes and frequencies over a large range of flow speeds and was also used to study the motion kinematics, whereas surface tracking was used to study how small-scale flatness defects and large-scale motion are related – in particular with respect to bistability and hysteresis.

2.1. Experimental facility

Flag flutter experiments were performed in a suction-type wind tunnel at Auburn University, which has a 244 cm × 61 cm × 61 cm square test section (please refer to § 2.6

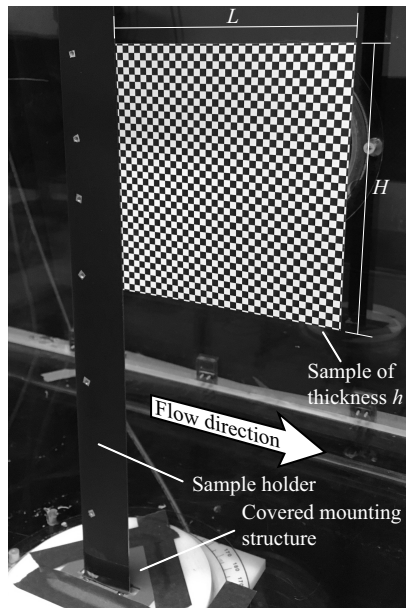


Figure 2. The sample holder with a sample in the wind tunnel. Picture mirrored for consistency with conventional flow direction from left to right: L length; H height.

for flow characterization). At approximately three quarters of the test section's length from its entrance, a sample holder spanned the test section vertically. The vertical configuration was chosen to minimize the effects of gravity through tensioning or bending. The sample holder consisted of two machined aluminium strips, the longer one of which was anchored to the test section at both ends whereas the shorter one was affixed to the longer one by means of eight flat-head screws. Together, the strips formed a streamlined body based on the SD8020-015-88 aerofoil with a chord length of 42 mm and a maximum thickness of 6 mm plus the thickness of whatever flag was clamped between them (figure 2). Spacers were used in the front part of the holder to keep both strips parallel. Through a tap test on the mast equipped with a 0.1 mm spacer, the lowest natural frequency and the associated damping ratio were computed to be 40 Hz and 0.011, respectively. The sample holder was sufficiently straight (Appendix A.1).

2.2. Samples

Flag samples were cut from various materials, with the main direction of curvature from manufacturing aligned axially so as to maximize transverse flatness. All had a free length of $L = 148.3$ mm (5.84") and a height of $H = 152.4$ mm (6"), which makes $H^* = 1.03$. Based on the resulting ratio of normal wall distance to flag length of 2.05 and the numerical results of Alben (2015), we do not expect the lateral test section walls to affect the stability and flutter characteristics of our flags. Based on Hiroaki & Watanabe (2024), also the vertical separation of the flags to the top and bottom of the test section is sufficient to exclude confinement effects.

The samples were all laser printed with a chequerboard pattern of 4.064 mm (0.16") pitch, which resulted in a grid of 37×38 trackable corner features. With this pitch we expect to capture the range of spatial frequencies relevant for hysteresis, while the random uncertainty associated with stereo motion tracking does not cause too much noise in the spatial derivatives obtained by finite differencing. Table 1 lists the mechanical properties

Identifier Material	CP1 copy paper	CP2 copy paper	CP3 copy paper	TE1 TerraSlate 5 mil (polyester)	TE2 TerraSlate 5 mil (polyester)	TP1 transparency (polyester)	TP2 transparency (polyester)	CS1 cardstock	CS2 cardstock	SS1 stencil sheet (polyester)	SS2 stencil sheet (polyester)
h (μm)	97	97	104	114	117	104	103	213	216	258	262
m (g m^{-2})	76	76	80	139	143	142	143	177	178	358	360
D (mN m)	0.16	0.17	0.21	0.47	0.49	0.55	0.57	1.94	2.1	6.84	6.74
μ	0.44	0.44	0.47	0.81	0.83	0.82	0.83	1.03	1.04	2.08	2.09
H/h	1579	1571	1465	1333	1303	1465	1481	715	706	591	583
Data sets	1	1	3	1	2	1	1	2	2	2	1

Table 1. Properties of flag samples: h , thickness; m , area density; D , plate bending stiffness; μ , mass ratio; H , flag height.

of all samples along with the number of data sets acquired. The plate bending stiffness of printed sheet stock was estimated from the tip displacement of strips cantilevered in a fixture, bending under their own weight. The fixture was flipped once to eliminate the influence of curvature inherent to the strips. Euler–Bernoulli beam theory provided the relationship between displacement and plate stiffness. By choosing appropriate strip lengths, care was taken to limit the tip slope. At rest, the tip of the flags deviated from the axial direction by angles of $0.5^\circ - 32^\circ$ due to inherent longitudinal curvature and gravity. The air flow eliminated any large curvature before the onset of oscillations, however, a possible impact on the results is discussed in § 3.4.

2.3. Motion tracking methods

Two complementary methods of motion tracking were employed, surface tracking from one side and edge tracking from below. For surface tracking, two VEO4K 990L cameras (Vision Research Inc.) were equipped with Nikkor 50 mm lenses set to an f-number of 16. They were vertically arranged as a stereo camera pair, the optical centres 36.23 ± 0.12 cm apart and the optical axes converging at an angle of $35.6^\circ \pm 0.7^\circ$. Vertical rather than horizontal arrangement was chosen for a better view during flutter. For edge tracking, a VEO 640L camera (Vision Research Inc.) was equipped with a Scheimpflug adapter and a Nikkor 50 mm lens set to an f-number of 2.8. The resolution was approximately 15 pixels mm^{-1} and 10–13 pixels mm^{-1} for surface tracking and for edge tracking, respectively.

Multiple high-power light-emitting diode (LED) arrays (MultiLED QX, GS Vitec GmbH) illuminated the flag for surface tracking. With transparent flags, a white surface behind the flag was illuminated instead. For edge tracking a single LED array was combined with two slits to illuminate only the lower edge. The LEDs were computer-controlled and turned on only during imaging to limit light-induced heating.

For calibration and data processing, MATLAB’s Computer Vision Toolbox was used. For the calibration of the stereo camera pair, laser-printed chequerboard patterns were applied to a precision-machined aluminium plate and waved in the volumetric region of interest (details in Appendix A.2). Also the edge tracking camera was calibrated by waving a chequerboard plate, and the plane that the flag’s edge would move in was calibrated with another chequerboard plate which was clamped to the sample holder.

The surface tracking images were processed by detecting the chequerboard pattern printed on all samples, using MATLAB’s gradient-based function `detectCheckerboardPoints`, and triangulation of corresponding features. The edge tracking images were processed with a MATLAB script that followed the path of highest image intensity.

Local surface curvature was approximated by means of the first and second derivatives of the surface's y -coordinate along the tracking pattern's principal directions. To reduce noise in figures of this document, the derivatives were evaluated on smoothing splines, whereas for Supplementary movies, they were computed directly. Gaussian curvature was computed as the product of both curvatures in this document, whereas for the movies, it was computed from the second fundamental form, which is independent of the coordinate system. All derivatives were computed via finite differencing. Uncertainties are detailed in [Appendix A.2](#). To quantify a flag's local bending stiffness, a polygonal cross-section with the flag's known thickness was reconstructed. The smaller principal second area moment, I , of the cross-section relevant for bending stiffness was calculated and normalized by I_{flat} , the value for a flat rectangular cross-section. A higher I/I_{flat} indicates greater bending resistance, with $I/I_{flat} = 1$ denoting minimal stiffness.

2.4. Wake flow visualization

The beam of a continuous green laser (RN-532nm-G1000, Beijing Ranbond Technology Co., Ltd.) was expanded to a sheet through two planoconcave cylindrical lenses. The sheet was aligned with a horizontally mounted chequerboard calibration plate, which was placed approximately 6 mm above the test section's centre line. As a tracer, fog from a fog machine (Z-800II, Antari Lighting & Effects Ltd.) operated with water-based liquid (Fog Worx, Sanco Industries, Inc.) was made to be ingested by the wind tunnel. A VEO 640L high speed camera (Vision Research Inc.) equipped with a Scheimpflug adapter and a 50 mm Nikkor lens (f-number 1.8) was pointed at the plate at an angle from below and calibrated by the same method as the edge tracking camera. The images were digitally reprojected to obtain a normal perspective. The observed area measured approximately 32 cm ($\approx 2.2L$) streamwise and 25 cm laterally, with a resolution of 5–7 pixels mm^{-1} . The flag's tip was visible on the images in most conditions.

2.5. Instrumentation, data acquisition and signal generation

The sample holder was equipped with a set of four strain gauges at each end that chiefly responded to lateral bending. In combination with two DMD4059 strain gauge to direct current isolated transmitters (Omega Engineering Inc.) they recorded the frequency content of structural vibrations. This helped monitor resonance between the structural vibrations due to the fan motor's drive (0–60 Hz), the sample holder and the sample. For the outcomes see [Appendix A.1](#). The airspeed, U , was measured with a pitot–static probe and a 1 INCH-G-4V pressure transducer (All Sensors Corporation). The tube was mounted 1.4 m upstream of the sample holder, 11 cm below the ceiling and 10 cm from the lateral wall. All data acquisition and signal generation was handled through a USB-6341 data acquisition device (National Instruments Corp.). The wind tunnel's fan motor was powered by an adjustable speed drive (Toshiba H7), controlled by an analogue signal.

2.6. Flow characterization and experimental conditions

The air density was computed from pressure, temperature and relative humidity. The turbulence intensity at the location of the sample holder was characterized through hot-wire anemometry, with the sample holder removed but the pitot–static probe in place. Right on the centre line, 10 cm above it, and 10 cm below it, the turbulence intensity was 0.5 % at 1 m s^{-1} , 0.3 % at 5 m s^{-1} and 0.25 % at 20 m s^{-1} . [Table 2](#) informs about the geometric blockage of the test section. At the critical airspeeds (between 3.2 m s^{-1} and 13 m s^{-1}), the Reynolds number based on the free flag length, Re_L , was in the range of 30 000 and 120 000, and between 8600 and 34 000 based on the chord length of the sample

	Blockage from swept area	Maximum instantaneous blockage
Maximum recorded flutter amplitude (76 mm)	7.2 %	4.1 %
Maximum flutter amplitude immediately after onset (61 mm)	5.8 %	3.4 %

Table 2. Blockage ratios caused by the sample holder and the fluttering flag from axial projection, at selected conditions.

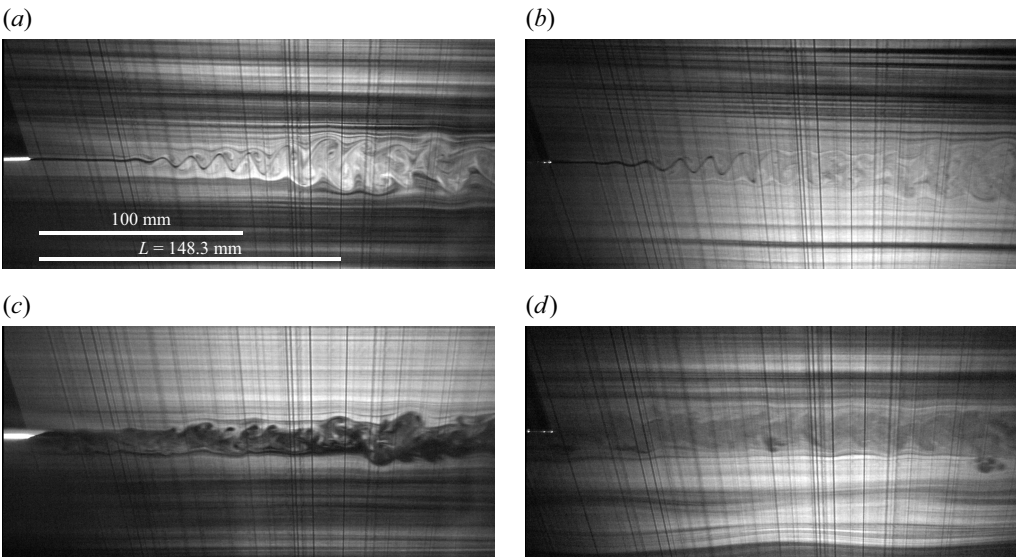


Figure 3. Examples of wake visualization for flow characterization. (a) Fully laminar at an airspeed of $U = 3.25 \text{ m s}^{-1}$ (TerraSlate sample TE1), (b) fully laminar at $U = 3.6 \text{ m s}^{-1}$ (transparency sample TP2), (c) turbulent on one side at $U = 4.35 \text{ m s}^{-1}$ (copy paper sample CP1), (d) fully turbulent at $U = 7.5 \text{ m s}^{-1}$ (stencil sheet sample SS2). The vertical dark lines originate from scratches on the acrylic test section wall. Here L is flag length. Sample identifiers refer to [table 1](#).

holder. From wake flow visualization during the non-fluttering state, evidently the flow just upstream of the flags' tip was fully laminar up to $U = 3.6 \text{ m s}^{-1}$. For $3.75 \text{ m s}^{-1} \leq U \leq 6 \text{ m s}^{-1}$, patches of disturbed smoke were visible or one side was turbulent and the other side laminar. For $U \geq 7.5 \text{ m s}^{-1}$, the flow on both sides was turbulent. Examples are presented in [figure 3](#).

Once a sample was clamped, the critical speeds were first explored through manual speed control. Then, an automated sequence of upsweep and downsweep with low acceleration rates determined the critical speeds more precisely. With those speeds, the stepwise velocity sweep for edge tracking was executed. At every step, we recorded a time series corresponding to roughly five flapping cycles based on the nominal flapping frequency determined before, with 60 images per cycle, which resulted in 600–1500 f.p.s. (frames per second). This was complemented by manually prescribing selected airspeeds for stereo tracking. We targeted recording a time series corresponding to at least five flapping cycles, with between 37 and 60 images per cycle, which resulted in 600–925 f.p.s. This test procedure was executed between one and three times for each sample, as indicated in [table 1](#). The samples were removed from the sample holder between executions, and executions of the same sample were on different days. We refer to the data obtained from

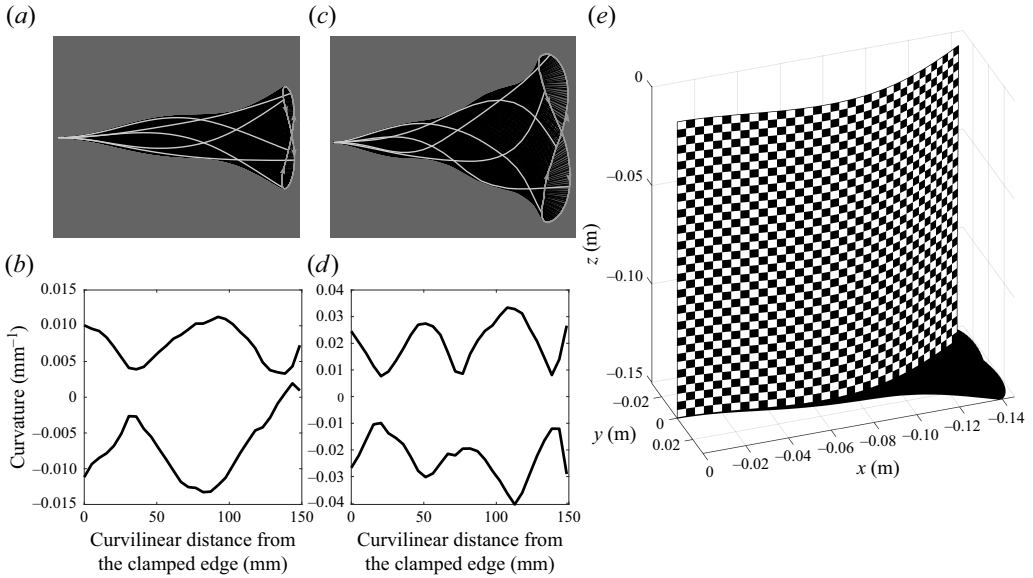


Figure 4. Visualization of motion tracking data from (a–d) edge tracking and (e) from surface tracking. (a,c) Superposition of edge shapes with five emphasized instances and highlighted path of the free end. (b,d) Envelopes of local curvature computed from the data of (a,c). (e) Reconstruction of the surface in one instance and superposition of all locations of the lower edge. (a,b,e) Cardstock sample CS1, (c,d) copy paper sample CP2 (refer to table 1).

one execution as one data set. For at least one sample per material, also wake visualization was done at the same conditions as stereo tracking.

3. Experimental outcomes

Here we present our motion tracking data and analyse it to obtain insight into the kinematics and into the connection between small-scale flatness defects and large-scale motion throughout a velocity sweep.

3.1. Flutter motion

Figure 4 illustrates typical motion tracking results. Most samples exhibited flutter in the lowest structural mode with only one neck (Eloy *et al.* 2008), as observed in figure 4(a). In contrast, copy paper samples exhibited two-neck flutter, illustrated in figure 4(c), as anticipated from the mass ratios reported in table 1. The motion contains elements of both standing and travelling waves, with the tip moving along a figure-eight path, mostly pointing away from its travel direction, shown in figures 4(a) and 4(c). Figures 4(b) and 4(d) display local curvature envelopes, highlighting mode shape differences via the number of waists. Supplementary movies 1–4 provide visualizations of edge tracking data. Figure 4(e) presents a three-dimensional (3-D) reconstruction of an instantaneous surface with the lower edge locations superimposed for context. Our method reconstructs the entire surface, excluding the outermost thin rectangles. Supplementary movies 5 and 6 animate the 3-D tracking for samples CS1 and TE2, respectively.

Figure 5 illustrates the tip amplitude variation through a stepwise velocity sweep. In the initial upswing from $U = 0 \text{ m s}^{-1}$, vibrations exhibit small amplitudes, sometimes appearing irregular or expressing a dominant frequency. For TE2, flutter initiates suddenly

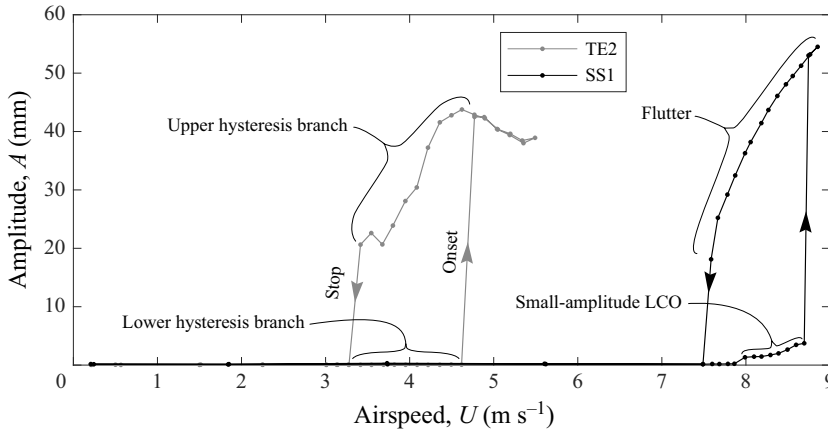


Figure 5. Evolution of tip amplitude throughout a stepwise velocity sweep of TerraSlate sample TE2 and stencil sheet sample SS1 (refer to [table 1](#)).

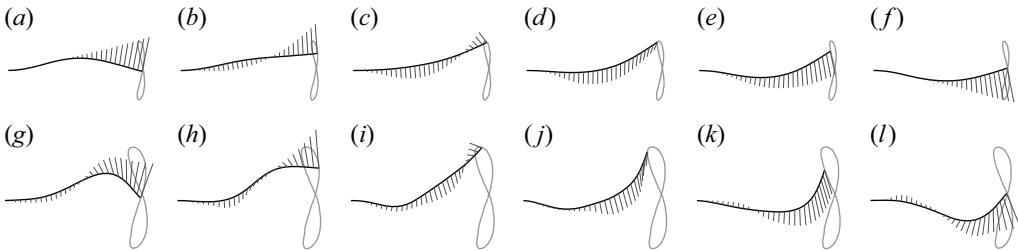


Figure 6. Kinematics of cardstock sample CS1 (*a–f*) and copy paper sample CP2 (*g–l*) over a half-cycle of flutter from edge tracking. The figure-eight tip path is indicated. Velocity vectors point into the local direction of motion. The vectors' scale is normalized per data set. For sample properties, refer to [table 1](#).

at a critical velocity, whereas SS1 shows small-amplitude LCO before flutter sets in, a pattern seen in most datasets. After transition to flutter, amplitudes change with increased velocity. During downsweep, amplitudes adhere to the upper hysteresis branch until flutter ceases. For TE2, amplitude changes are less smooth compared with SS1, possibly due to kinks that travel diagonally across the flag once per motion cycle, introducing irregularity in the motion (see Supplementary movies [2](#) and [6](#)). Each data set displays a distinct amplitude plot shape (refer to Supplementary [figure S1](#)). Modes during small-amplitude LCOs differ markedly from flutter, featuring transverse bending, longitudinal twisting and asymmetry, except in SS1 and SS2, where similarity exists, yet accompanied by snap-through events (see Supplementary movie [7](#)).

To further elucidate the flutter kinematics and form conjectures about how the flag exchanges energy with the flow, crucial for our ODE model, [figure 6](#) illustrates the motion depicted in [figure 4\(a,c\)](#) for a half-cycle of flutter with superimposed velocity vectors. Drawing from Connell & Yue (2007), we consider the pressure field as a potential energy reservoir exchanged with the flag's kinetic energy. Although we lack pressure data, the flag segment's local curvature and travel direction permit qualitative insights into the adjacent pressure field. In one-neck flutter ([figure 6a–f](#)), the tip's figure-eight path correlates with a curvature reversal over a significant flag portion ([figure 6a–c](#)) before motion reverses ([figure 6c,d](#)). In two-neck flutter ([figure 6g–l](#)), the first section of the

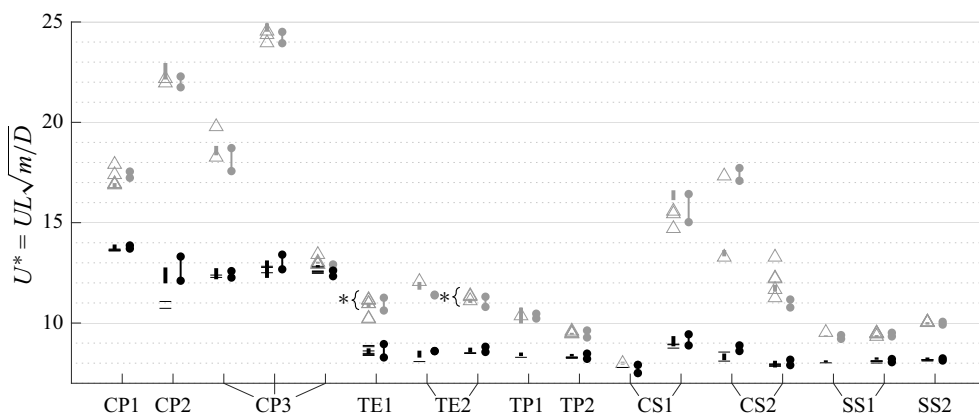


Figure 7. Reduced airspeed U^* of flutter onset (U_c^* , grey symbols) and of flutter stop (U_d^* , black symbols) for all samples. Thick vertical lines demarcate uncertainty from stepwise speed increments during edge tracking. Triangles and horizontal lines are from continuous velocity sweeps. Vertically stacked dots with connecting lines mark the intervals in which transition happened during 3-D tracking. Data sets are roughly sorted by increasing mass ratio. Data set labels refer to table 1. Two onset speeds from continuous sweeping marked with an asterisk had frequency matching between fan motor drive and flag vibrations (refer to Appendix A.1). Here U is airspeed, L flag length, m area-specific mass, D plate bending stiffness.

flag often bends oppositely to the second section. Thus, in both modes, large portions of the flag predominantly move towards the convex side. If convex and concave areas experience negative and positive pressures, respectively (Thoma 1939), the pressure field mostly exerts positive work on the flag. For the purpose of modelling in § 4, we will assume that fluid forcing on the flag works all the time from one reversal to the other, and always in the direction of motion.

Taneda (1968) noted that the transverse oscillations are phase-shifted at the flag's rearmost sections, causing waves to move backward. Near the tip, an instantaneous upward deflection occurs with significant upward bending; during reversal (figure 6c,i), the velocity is directed towards the flag's concave side with a major upstream component. This indicates the flag loses energy to the flow as it opposes the pressure field. However, the flag may recover some energy from the pressure field on adjacent sections moving in the opposite direction (figure 6c,i) and on the tip itself after reversal (figure 6d,j). These observations will be revisited when introducing the ODE-based model in § 4.

3.2. Critical airspeed and repeatability

Figure 7 presents the reduced airspeeds for both flutter onset (U_c^*) and stop (U_d^*) across all data sets, which are approximately arranged by increasing mass ratio. Data were gathered from continuous and stepwise velocity sweeps, and 3-D tracking. Consistent with Eloy *et al.* (2012), the stop speed (black) shows greater consistency across similar experiments than the onset speed (grey). The lighter copy paper samples, CP1, CP2 and CP3, exhibit a higher stop speed U_d^* due to experiencing two-neck flutter.

Most data sets exhibit consistent internal agreement across repetitions. However, copy paper and cardstock samples display notable variability across data sets, even when the same sample is tested. This variability is mainly attributed to humidity imbalances between the air and the sample, causing mild deformation during experiments. Factors such as minor clamping differences and possible plastic deformations during handling and storage may also contribute. Despite this, conclusions regarding the correlation between shape and flutter hysteresis behaviour remain valid since the 3-D flag shape is assessed each time.

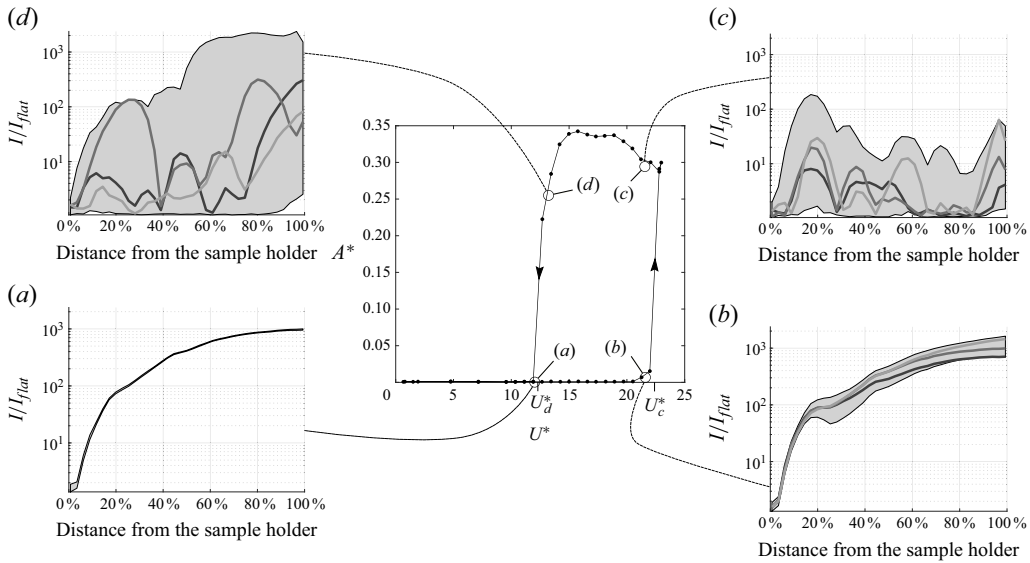


Figure 8. Reduced amplitude, A^* , from edge tracking as a function of reduced airspeed, U^* , throughout a velocity sweep. (a–d) Envelope (shaded area) of normalized cross-sectional stiffness, I/I_{flat} , from surface tracking and instantaneous distributions (lines) at three instances. Data of sample CP2 from [table 1](#).

The highest repeatability across data sets was observed with the thickest plastic samples, SS1 and SS2.

3.3. Analysis of cross-sections throughout a velocity sweep

[Figure 8](#) illustrates how the normalized tip amplitude, $A^* \equiv A/L$, varies with the reduced airspeed, $U^* \equiv UL\sqrt{m/D}$, during a velocity sweep employing edge tracking. The sample, CP2, exhibits an 82 % relative hysteresis loop extent, defined as $\mathcal{E} \equiv (U_c - U_d)/U_d$. Locations (a) to (d) on this loop, close to transitions between static and fluttering phases, were captured using stereo motion tracking, with 230 frames per location at 920 f.p.s. – translating to six and three flapping periods for states (c) and (d), respectively. In state (c), due to instantaneously shallow view angles at the flapping tip, approximately 8 % of frames could not be reconstructed, but this is unlikely to significantly affect the findings. [Figures 8\(a\) to 8\(d\)](#) display statistics for the normalized stiffness, I/I_{flat} (defined in § 2.3), along the sample. The shaded grey area reflects the full time series' envelope, and the lines depict example instantaneous distributions.

At point (a), no periodic motion is observed, only vibrations with varying amplitudes around 0.03 mm and approximately 45 Hz. The large transverse curvature, corresponding to a cross-sectional tip thickness of approximately 3 mm, results in significantly greater stiffness compared with a flat sheet of copy paper. While the sample holder enforces a straight clamped edge, the stiffness increases monotonically towards the free end. At point (b), aperiodic motion is noted but flutter remains suppressed. The wider envelope of I/I_{flat} signifies vibrations, yet retains the same shape as in (a). Point (c) is on the upper hysteresis branch, at the same velocity as (b). Here, flutter coexists with local flag flattening, allowing the envelope to approach 1.0 along much of its length, although flattening may occur momentarily only at selected points. For point (d), on the upper branch near the flutter stop, the envelope is higher than at (c), with local I/I_{flat} akin to the motionless state, (a). Complete flattening occurs except along the last 10 % of the length. Similar observations are applicable to all data sets except those lacking significant

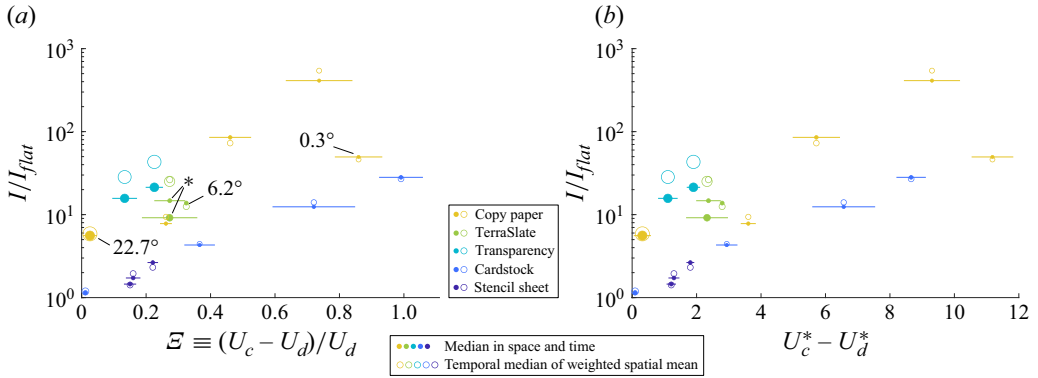


Figure 9. Correlation of flatness defects and hysteresis. Two metrics of normalized cross-sectional stiffness, I/I_{flat} , in a representative non-fluttering state versus (a) $E \equiv (U_c - U_d)/U_d$ and (b) reduced velocity difference, $U_c^* - U_d^*$. Marker size indicates the deviation of a tangent to the flag tip from the wind tunnel axis in quiescent air, with some data points labelled for reference. Horizontal lines demarcate uncertainty in hysteresis (only one per data set). Two data sets marked with an asterisk had frequency matching between fan motor drive and flag vibrations before onset (refer to Appendix A.1). Here U_c is onset speed, U_d stop speed, U^* reduced airspeed as defined in (1.1).

hysteresis or using stencil sheets (explained further below). These findings support the hypothesis that stiffness-inducing flatness defects are diminished during flutter but not on the lower hysteresis branch, likely contributing to hysteresis as explained by Eloy *et al.* (2012). Supplementary movies 8 and 9 provide animations of points (b) and (d) of figure 8, respectively, also illustrating several cross-sections.

The stencil sheet samples with $h = 0.26$ mm, the thickest and heaviest in the study, exhibit a small-amplitude LCO with A between 1.9 – 3.7 mm before flutter occurs (e.g. see sample SS1 in figure 5). This phenomenon appears unaffected by transverse curvature as the I/I_{flat} envelope reduces to 1.0 like in figure 8(c). This was observed consistently across all three data sets using this material (see table 1). It remains unclear if the same physics apply here as for other samples or if our I/I_{flat} criterion is inadequate. The sample holder's finite rigidity is likely not a factor, given the flag root's minor lateral vibration, approximately 0.1 mm in amplitude. We opted not to investigate this case further but note that Tang *et al.* (2003) observed a similar LCO state in an aluminium panel with a low height-to-thickness ratio of $H/h \approx 325$ and H^* of 0.48 (for reference compare with our table 1), and suggested aerodynamic nonlinearities might cause distinct small- and large-amplitude LCO states. Conversely, Hiroaki & Watanabe (2024) found no hysteresis for flags with $0.3 \leq H^* \leq 1.17$, $120 \leq H/h \leq 470$, $\mu \approx 2.9$.

3.4. Correlation between flatness defects and onset delay

To explore the relationship between increased stiffness due to flatness defects and onset delay, we analyse two statistical metrics of I/I_{flat} in representative non-fluttering states (e.g. point (a) in figure 8), derived from time series surface tracking data.

- The median across all locations and instances, noted for its resistance to outliers.
- The temporal median of the weighted sum of I/I_{flat} , using local curvature variation during flutter as weights. This variation is the envelope height of curvature, shown in figure 4(b,d). Although edge tracking data appear in the figure, here we use surface tracking.

The second metric assumes that stiffness of locations experiencing higher bending in each sample's mode shape (two necks in copy paper, one neck in others) has more effect.

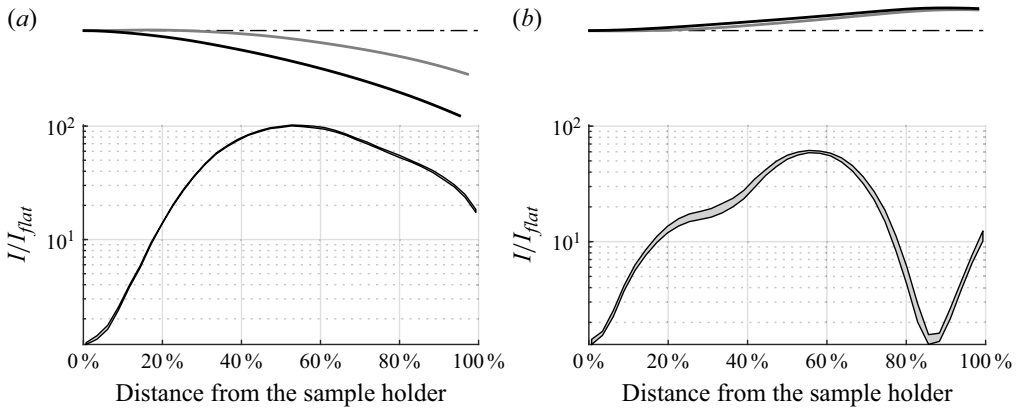


Figure 10. Straightening of an initially curved flag. (a) Quiescent air, (b) airspeed close to the speed where flutter stops (not fluttering). Above the graphs are the vertical projection of the shape of the flag's upper edge (black) and lower edge (grey) with the ideally straight shape (dash-dotted). The left-hand end is clamped. The graphs are the envelope of normalized cross-sectional stiffness, I/I_{flat} , from surface tracking. Data of transparency sample TP2 (refer to table 1).

Since non-fluttering states exhibit minor motion, using temporal median, average or minimum is not impactful. Figure 9 plots these metrics against \mathcal{E} and $U_c^* - U_d^*$ as hysteresis metrics. Critical airspeeds are derived from 3-D or edge tracking (see figure 7), which explains high hysteresis uncertainties in some data points. All four combinations of these metrics indicate a positive correlation between the width of the hysteresis loop and the increase in stiffness due to transverse flatness defects.

Four data points with low hysteresis but relatively high I/I_{flat} exhibit a flag shape with pronounced longitudinal curvature in still air, illustrated by larger markers in figure 9. Upon increasing the airspeed from $U = 0 \text{ m s}^{-1}$ to the non-fluttering state, the flag shape changes, as depicted in figure 10. While I/I_{flat} remains largely consistent in magnitude during this alignment in all four cases, the resulting S-shape might be related to low hysteresis. Alternative flatness metrics, potentially better than I/I_{flat} , could enhance the correlation by considering the entire 3-D surface rather than cross-sectional views.

Figure 11 illustrates how flatness defects affect similar samples by showing the tip amplitude evolution (above the coloured panels) for samples CS1 ($\mathcal{E} \approx 0.02$) and CS2 ($\mathcal{E} \approx 0.37$), along with their longitudinal, transverse and Gaussian curvatures. This is observed in two states: still near stop speed (figure 11a,c) and during flutter at similar amplitudes (figure 11b,d). In CS1's 'still' state (figure 11a), the tip vibrates with an amplitude of 0.2 mm at 14 Hz, while CS2 (figure 11c) shows aperiodic motion at 0.1 mm. During flutter, the longitudinal curvature greatly exceeds transverse curvature, displaying a smooth banded pattern. Consequently, Gaussian curvature – the product of the principal curvatures – is similar to the transverse curvature masked by multiplication with the longitudinal curvature. Here CS1 is relatively flat before flutter, shown by low transverse curvature (left-most column, central subpanel). The transition between states involves gradual amplitude changes and minor hysteresis. Conversely, CS2 exhibits significant transverse curvature (figure 11c), which disappears during flutter except at the lateral edges (figure 11d). Differences in transverse curvature account for differing onset speeds, and the reduction of curvature during flutter explains similar stop speeds. Supplementary movie 7 shows animations just before flutter onset of CS1 and CS2, and movie 5 depicts CS1's hysteresis loop.

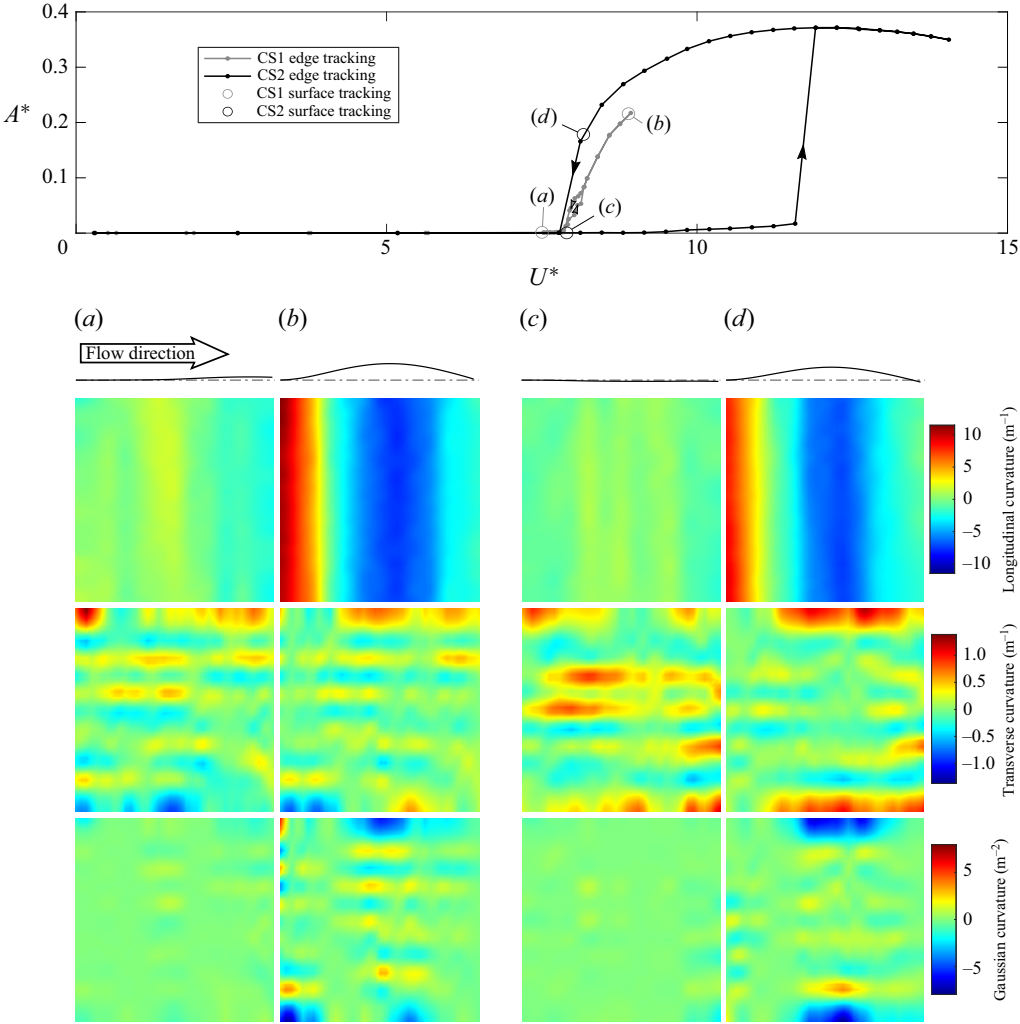


Figure 11. Reduced tip motion amplitude, $A^* \equiv A/L$, of cardstock samples CS1 and CS2 as a function of reduced airspeed, U^* (defined in 1.1) (above the coloured panels) together with metrics of instantaneous curvature for CS1 (*a,b*) and CS2 (*c,d*) in still (*a,c*) and flutter (*b,d*) states. The sample holder is located at the left-hand edge of each tile. From top to bottom are the vertical projection of the shape of the flag averaged along the span, longitudinal curvature, transverse curvature, Gaussian curvature. Here A is amplitude, L flag length. Sample identifiers refer to table 1.

The motion tracking data showed small areas of fluctuating transverse and Gaussian curvature in the centre of the sample during flutter, likely from measurement error (noting the 0.3 rad m^{-1} uncertainty described in Appendix A.2). However, negative Gaussian curvature consistently appeared at the lateral edges when longitudinal bending was large, in all samples. This suggests transverse bending towards the large-scale convex side, possibly due to Poisson's effect, where the concave side's compression and convex side's stretching are slightly offset by transverse bending at the edge. Therefore, it may not be completely accurate to claim that Gaussian curvature incurs a prohibitively high energetic cost in flag bending, as Eloy *et al.* (2012) argued.

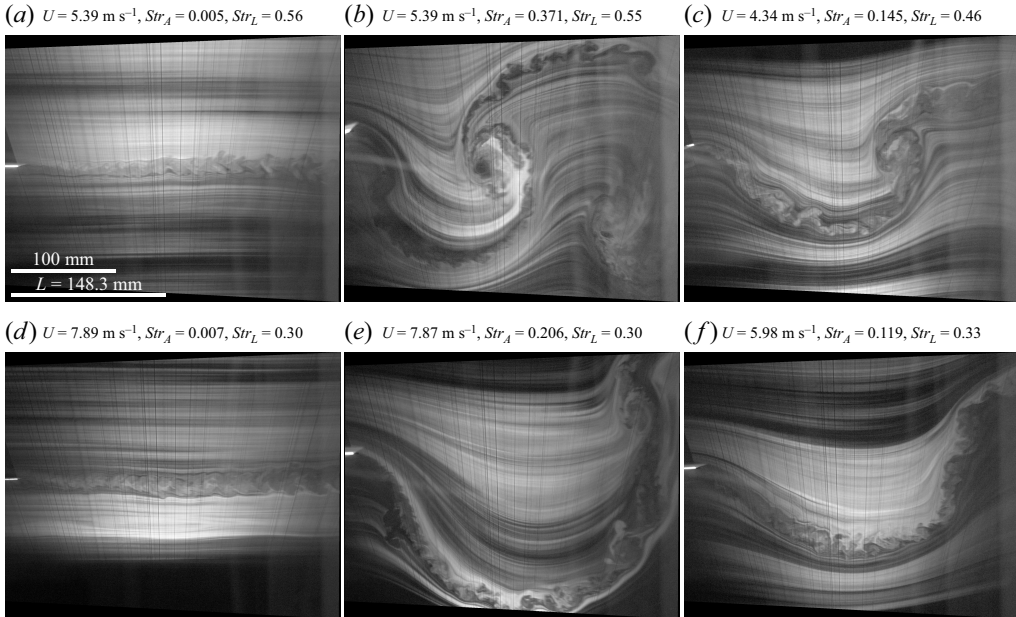


Figure 12. Flow visualization of wake structure. (a–c) copy paper sample CPI; (d–f) cardstock sample CS2. (a,d) Here U just below onset speed, not fluttering; (b,e) nominally same U as (a,d), fluttering; (c,f) U just above stop speed, fluttering. Here L is flag length, U airspeed, $Str_A \equiv 2fA/U$, $Str_L \equiv fL/U$, A tip amplitude, f flutter frequency. Within each row, the instant (or phase angle) within the motion cycle is approximately the same. Sample identifiers refer to [table 1](#). See also Supplementary movie [10](#).

3.5. Wake flow visualization

[Figure 12](#) presents a series of wake flow visualizations of a light copy paper sample ([figure 12a–c](#)) and a heavier cardstock sample ([figure 12d–f](#)). [Figures 12\(a,b\)](#) and [12\(d,e\)](#) show airspeeds just below U_c , contrasting the lower and upper hysteresis branches. Although frequency or $Str_L \equiv fL/U$ is similar, the amplitude, characterized by $Str_A \equiv 2fA/U$, differs significantly. [Figures 12\(c\)](#) and [12\(f\)](#) display flutter occurring at airspeeds slightly above U_d , with [figure 12\(f\)](#) matching the conditions in [figure 11\(d\)](#). On the lower branch ([figure 12a,d](#)), small-amplitude vibrations do not cause vorticity roll-up in the near wake, unlike during flutter where vortices roll up. The value of Str_A indicates the tip displacement to advection distance ratio per period of motion, with higher Str_A typically leading to tighter wake curves and discrete vortex formations. However, this is not always true across different mass ratios. For example, [figure 12\(c\)](#) shows a dominant vortex, while [figure 12\(e\)](#) with higher Str_A has multiple weak vortices, suggesting that the mode shape variance may play a role. These findings suggest the wake may contribute to hysteresis, as discrete vortices, thought to amplify flag motion, are absent in small-amplitude LCO ([figure 12a,d](#)). However, during flutter close to U_d , as in [figure 12\(f\)](#) no dominant vortex formation was observed with any but the lightest material, as in [figure 12\(c\)](#). Consequently, pressure feedback from the vortical wake is unlikely to sustain flutter in heavier flags, correlating with the assertion of Hiroaki & Watanabe (2024) that vortex formation is less important as a source of aerodynamic nonlinearity that contributes to bistability. See Supplementary movie [10](#) for a moving version of [figure 12](#).

As a secondary observation we note that sometimes the boundary layer state on both sides of the flag appears to alternate between laminar and turbulent, as in [figure 12\(e,f\)](#). Namely, the advancing side (above the flag tip in the figure) has laminar flow, while the

retreating side (below the tip) is turbulent. This may be related to the pressure gradient along the flag, which is adverse on the retreating side which has relatively high pressure towards the tip and favourable on the advancing side which has relatively low pressure towards the tip.

4. An ODE-based model for flag flutter

In light of the experiments and in order to validate our understanding of the physics, here we propose a model of flag flutter that consists of a single ODE and justify its form based on the published literature and on our own experimental results. We model the flag flutter phenomenon as an oscillator with variable stiffness and a forcing function that depends on both motion direction and instantaneous deflection. This approach aims to qualitatively replicate the bistability observed in experiments, attributed to flatness defects; it is not meant to predict critical velocities, amplitudes or frequencies from physical flag properties. Although wake effects were suggested as a potential source of hysteresis (Tang & Païdoussis 2007), we did not include them in the model to isolate only the effects of flatness defects, which are more significant. Future model developments may incorporate explicit wake representation as part of the forcing. Before devising this single-equation model, we explored a combination of a structural oscillator and a nonlinear wake oscillator, similar to the VIV model of Facchinetti *et al.* (2004). However, due to the complexity of that alternative, its challenging parameter justification and parallel oscillator behaviour over velocity sweeps, we opted for the current model. Note that while VIV models like the one of Facchinetti *et al.* (2004) involve a van der Pol oscillator (for modelling a bluff-body wake), this is unsuitable for our model where unconditional self-excitation is undesirable.

The ODE-based model for flag flutter is proposed in the following form:

$$\ddot{Y} + 2\zeta\dot{Y} + (1 + \chi N(\alpha, \beta, Y/Y_{ref}) - \gamma Y^2)Y = \text{sgn}(\dot{Y})U|Y| + E \sin(\omega_e \tau), \quad (4.1)$$

$$N(\alpha, \beta, \hat{Y}) = \frac{1 - \frac{1}{1 + \exp(\alpha - \beta \hat{Y}^2)}}{1 - \frac{1}{1 + \exp(\alpha)}}. \quad (4.2)$$

This is a second-order ODE in Y with dimensionless time, $\tau \equiv \omega_0 t$, as the independent variable, where t is dimensional time and ω_0 is the dimensional natural angular frequency of the unforced oscillator with constant stiffness ($\chi = 0$, $\gamma = 0$) and without damping, $(d^2/dt^2)Y + \omega_0^2 Y = 0$. Here Y represents some measure of the instantaneous deflection of the flag in arbitrary units, and we will interpret it as the lateral tip displacement. Here ζ is the damping ratio. Since τ is used rather than dimensional time, the dimension of the equation is that of Y (a length) and the restoring force term contains no stiffness parameter; rather, the baseline stiffness is always unity.

Here χ , α , β and Y_{ref} parametrize a zone of increased stiffness (an upside-down ‘notch’) in a neighbourhood of $Y = 0$, where χ is the additional stiffness at $Y = 0$, Y_{ref} determines the extent of the neighbourhood and the combination of α and β determines the functional shape of the stiffening, $N(\alpha, \beta, \hat{Y})$. We call N the notch function, and its product with χ the notch term. The numerator of N is a two-sided logistic function. The division by $1 - (1/(1 + \exp(\alpha)))$ ensures that the stiffness at $Y = 0$ is $1 + \chi$ for any choice of α . The parameters α and β are constrained by the condition

$$N(\alpha, \beta, 1) = c \Leftrightarrow \beta = \alpha - \ln \left(\left(1 - c \left(1 - \frac{1}{1 + \exp(\alpha)} \right) \right)^{-1} - 1 \right), \quad (4.3)$$

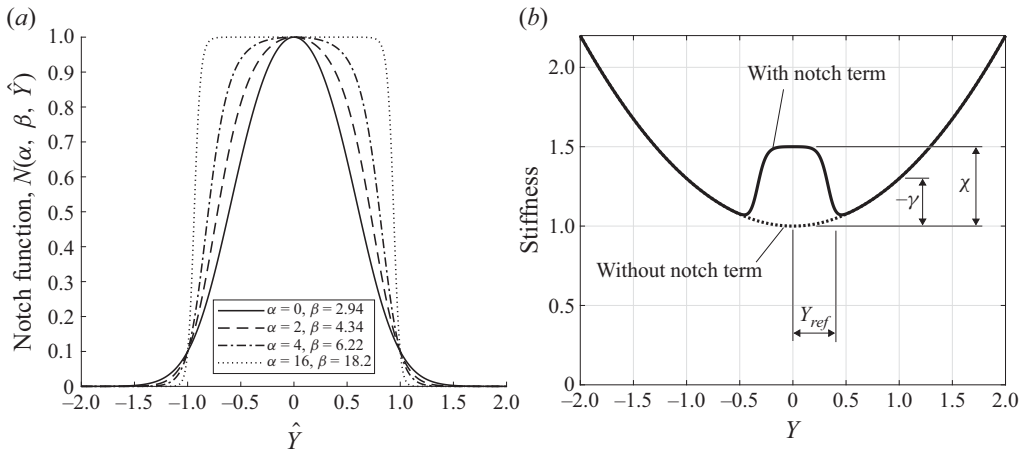


Figure 13. Visualization of the stiffness term of the ODE-based model. (a) The shape of the notch function, $N(\alpha, \beta, \hat{Y})$ (4.2), for various values of the constants α and β , where $\hat{Y} = Y/Y_{ref}$. (b) exemplary variation of stiffness with deflection, Y , with the defining algebraic constants: notch half-width Y_{ref} , notch height χ , coefficient of quadratic stiffening γ .

which enforces that the stiffness at $Y = Y_{ref}$ is $1 + \chi c$, with c a small number. We use $c = 0.1$ throughout this paper. Figure 13(a) visualizes the family of functions that is parametrized by α . Small α yield gradual transitions, whereas larger α yield abrupt transitions. This choice of N enables us to explore the effects of the flank slope in § 5.3. For $\alpha \rightarrow \infty$, N becomes rectangular. The notch term is used to model the stiffening effect of flatness defects present in a flag. As shown by means of figure 8(a), before onset the stiffness of a physical flag with inherent transverse curvature is larger than what it would be if the flag were flat. During small-scale motion just below the onset speed, the stiffness does not change much (figure 8b). But after onset of flutter, cross-sections are locally flattened by longitudinal bending such that the lower edge of the stiffness envelope reaches close to 1.0 (figure 8c,d). It is, however, not low everywhere simultaneously. A given cross-section may experience both curved (stiffer) and straight (less stiff) moments, while there is always some location with low stiffness at a given instant. We transfer these experimental observations into the ODE model through the notch term, which makes the oscillator stiffer when it is instantaneously located at low $|Y| < Y_{ref}$, such that onset is inhibited. Although one could arguably want to deactivate the notch term altogether during flutter, we do not opt to do so and justify this with the fact that the real flag senses some residual effect of flatness defects also during motion. Moreover, it would be hard to justify the conditions for deactivation and reactivation. We'll show later that the presence of the notch has none but a minor effect on the large-amplitude oscillation dynamics when U is large, just like the transverse curvature changes little about the flutter amplitude in Eloy *et al.* (2012) (their figure 2).

The hardening term, $-\gamma Y^2$, results in quadratic stiffening with Y , as in a Duffing equation. This term is required to prevent unbounded amplitude growth at large flow speeds and to let the oscillation frequency grow with increasing flow speed, as witnessed by fairly constant Strouhal number, fL/U , in experiments (refer to figure 12 or Yu *et al.* (2019)). It is consistent with the idea that dynamically induced tension in the flag limits its amplitude, as suggested for fully flexible flags by Moretti (2004), but we rather motivate it with the restoring force from the pressure field that acts on the tip of the flag at reversal to take up kinetic energy, this force presumably being greater at higher amplitudes. Note that

Connell & Yue (2007) made an analogy to a Duffing oscillator to explain the hysteresis of flag flutter (in two dimensions); they suggested that the flag behave like a softening spring ($\gamma > 0$), whereas we always set $\gamma < 0$, which corresponds to a hardening spring as required for a bounded large-amplitude LCO as discussed at the end of this section. Figure 13(b) visualizes the variation in stiffness with Y for $\chi = 0.5$, $\alpha = 4$, $\beta = 6.22$, $Y_{ref} = 0.4$ and $\gamma = -0.3$. In the vicinity of the notch flanks, $|Y| \approx Y_{ref}$, the stiffness drops, which causes the stiffness term to behave as a softening spring for small deflections, in line with Connell & Yue (2007). As an interesting observation we note also that Tang *et al.* (2003) mentioned that in their model, nonlinear terms related to mass inertia act like a cubic spring that reduces the LCO amplitude. Likewise in our model the cubic spring, $-\gamma Y^3$, limits the LCO amplitude, although the physical consideration behind this term is different.

The first term on the right-hand side models the nonlinear fluid forcing with U , the flow speed. While we acknowledge that, intuitively, the flow speed should appear squared as in dynamic pressure, $(1/2)\rho_f U^2$, the dependency on U^1 produces the desired square-root dependency of the limit cycle amplitude on the flow speed, as will be shown in § 5.1. The fluid forcing scales with the magnitude of the instantaneous deflection of the oscillator, $|Y|$. This is motivated by the idea that a straight (and steady) flag experiences no lateral force from the flow, and that the pressure forcing grows with deflection through high pressure in the troughs and low pressure on the crests (Thoma 1939). In combination with the notch term that stiffens the oscillator for small $|Y|$, this results in the desired bistability as will be shown in § 5.2. Intuitively, one may expect that the relatively high stiffness within $-Y_{ref} < Y < Y_{ref}$ results in larger restoring forces than the fluid forcing $\text{sgn}(\dot{Y})U|Y|$ is able to overcome unless U is large; we will disprove this idea when we analyse the mechanism of hysteresis in § 5.2. The term $\text{sgn}(\dot{Y})$ ensures that the forcing always acts in the direction of motion, inspired by the observations in the kinematics of flag motion in § 3.1. Note that the fluid forcing term can be brought to the left-hand side of the equation and interpreted as a modification to the stiffness, which then becomes $1 + \chi N(\alpha, \beta, Y/Y_{ref}) - \gamma Y^2 - \text{sgn}(Y)\text{sgn}(\dot{Y})U$. We do not model vortex shedding and the corresponding feedback on the flag. Based on our discussion in § 3.5, vortex shedding is not likely an essential nonlinear aerodynamic term for hysteresis.

The second term on the right-hand side is a harmonic excitation with E , the small excitation amplitude and ω_e , the frequency ratio between the excitation and the undamped natural frequency of the oscillator for $\chi = 0$ and small deflections, ω_0 . The sole purpose of the harmonic excitation term is to push the oscillator out of the initial condition where $Y = 0$ and $\dot{Y} = 0$. It can be seen as a representation of small fluctuations present in the incoming flow, or alternatively for structural vibrations in the flag's support, that might trigger the instability.

Unlike in two-equation models for VIV, where a distinct wake oscillator is coupled to a structural oscillator, in our model fluid and structure are represented by the same terms. The inertial term \ddot{Y} includes the structural inertia and any added mass, the damping term $2\zeta\dot{Y}$ includes both structural damping and fluid-caused damping (e.g. through convective loss of kinetic energy into the wake), the hardening term $-\gamma Y^2$ represents both flag kinematics (finite length, tension induced by centrifugal acceleration) and the conservative portion of the pressure field, the fluid forcing term represents the fact that the net energy flow from the pressure field to the flag is positive thanks to the flag's non-symmetric motion pattern.

Although we are aware of the closeness of solid and fluid time scales as elaborated in § 1.1, the fluid forcing does not contain the magnitude of \dot{Y} , which makes it a quasisteady

forcing term, and likewise the hardening term $-\gamma Y^2$ depends only on the instantaneous deflection. On the other hand, the damping term does not include the flow speed. Despite these apparent conceptual shortcomings, we will demonstrate a satisfactory model behaviour.

With $U > 0$, the ODE model has a large-amplitude limit cycle only if $\zeta > 0$ and $\gamma < 0$, i.e. if damping is positive and the spring's stiffness grows quadratically with displacement. If $\zeta = 0$, even with $\gamma < 0$, the oscillation grows beyond any bounds because the $\text{sgn}(\dot{Y})U|Y|$ term keeps adding energy to the oscillator and that energy has no dissipation mechanism. Also if $\zeta > 0$ but $\gamma = 0$, Y grows beyond any bounds if U exceeds some threshold which depends on ζ and χ . Beyond this threshold, if $U > 1$, the effective stiffness of the remaining spring term, $1 + \chi N(\alpha, \beta, Y/Y_{ref}) - \text{sgn}(Y)\text{sgn}(\dot{Y})U$, can become negative such that Y diverges monotonically. If alternatively $0 < U < 1$, the effective stiffness never drops below zero and an oscillation is sustained whose amplitude grows exponentially beyond any bounds. Conversely, if $\zeta > 0$ and $\gamma < 0$, the amplitude is limited for any $U \geq 0$ because beyond the amplitude of the limit cycle, A , the dissipation grows faster than the energy input as will be shown in § 5.2.

The parameter set $\zeta = 0.1$, $\chi = 0.5$, $\alpha = 4$, $Y_{ref} = 0.4$, $\gamma = -0.3$, $E = 10^{-5}$, $\omega_e = 0.1$ represents a reference configuration from which the effects of parameter variations will be explored. For the first five parameters, these values are chosen because they result in a nominally flag-like system behaviour as presented in § 5.1, with a similar evolution of amplitude as seen in sample SS1 (figure 5). The values of the last two parameters are the result of the sensitivity analysis presented in Appendix B. Please refer to that appendix also for details on numerical solution methodology, the simulation of incremental velocity sweeps, and the determination of critical speeds through bisection.

5. Model analysis

Here we present the behaviour of the ODE model, explain it, and explore its parameter space, to assess its ability to reproduce key aspects of the physical system.

5.1. The qualitative behaviour of a reference configuration

Figure 14 illustrates the model's reaction in the reference configuration to a stepwise increase and subsequent decrease in velocity. The labelled points on the central amplitude plot correspond to time-domain satellite plots. With χ at zero instead of 0.5, the amplitude response, indicated by the grey dashed line, shows no hysteresis.

At $U = 0$ (point (a)), low amplitude oscillations at the forcing frequency ω_e (refer to (4.1)) are noted. As U rises, oscillations at a frequency of approximately $\sqrt{(1 + \chi)}$ emerge and grow, as seen in points (b) and (c). Until just before the critical flutter speed U_c , the amplitude stays under 10^{-4} . Slightly exceeding U_c , the amplitude begins a gradual increase until it matches Y_{ref} , where it escalates sharply, leading to significant flutter oscillations, shown in figure 14(d). With further increase in U , the amplitude continues to increase, seen in figure 14(e). During downsweep, for $U > U_c$, the amplitude mirrors the upsweep behaviour. For $U_d < U < U_c$, it remains high without any discontinuity at U_c , shown in figures 14(f) and 14(g). In this velocity range, the system is bistable, which manifests as hysteresis. Only when U decreases below the stop speed U_d , the model returns to the non-fluttering state with low-amplitude oscillations, seen in figure 14(h). During this transition, the amplitude decreases rapidly once it reaches Y_{ref} .

In the fluttering state, the amplitude increases roughly as $(U - U_n)^{0.6}$ (refer to figure 14 inset), where U_n is the critical speed for a notchless oscillator, and the stiffening notch

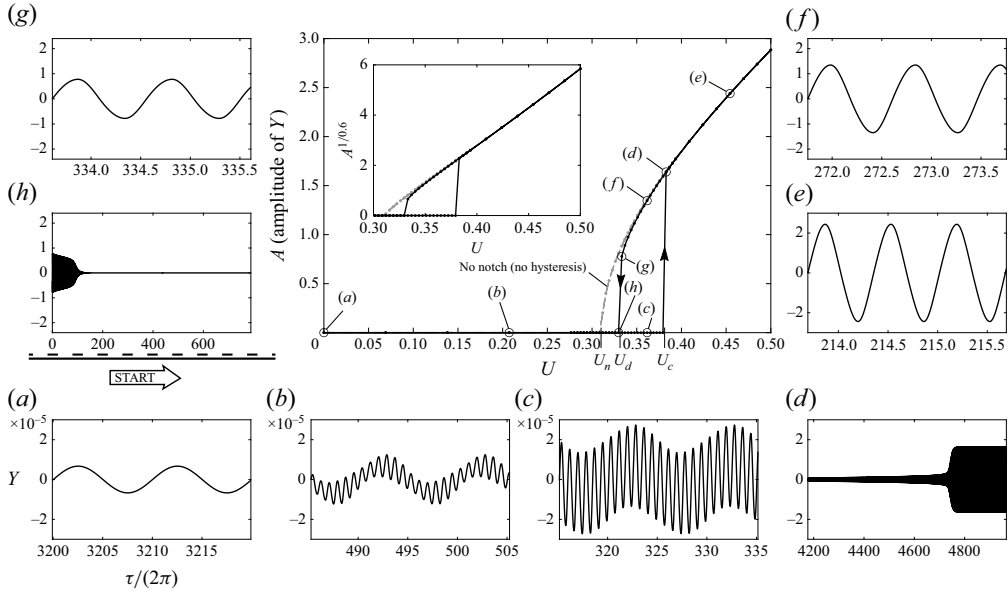


Figure 14. Response of the reference configuration of the model in terms of limit cycle amplitude, A , (main panel) and corresponding time histories (a – h). Here τ is dimensionless time, Y position of the oscillator, U flow speed, U_c critical speed of flutter onset, U_d critical speed of flutter stop, U_n single critical speed of the notchless oscillator. In the main panel, small dots mark the data points. When the notch term is (de-)activated, the amplitude follows the (grey dashed) black line.

term has minimal effect (see the grey dashed line for comparison). This parallels the findings of Eloy *et al.* (2012), though they used $\sqrt{U^* - U_c^*}$ (or maybe $\sqrt{U^* - U_d^*}$ as appears from their figure 2d and table 2) for curve fitting. Approaching U_d on the upper branch, the amplitude is smaller compared with the notchless oscillator. As observed in experiments, transitions between states are marked by discrete amplitude jumps (figure 8). The amplitude plot resembles sample SS1 (figure 5), but in the ODE model, lower branch amplitudes do not reach macroscopic levels. Also, see Eloy *et al.* (2008), figure 2, for a similar experimental hysteresis loop. Note that with $\chi = 0$, a continuous amplitude increase is observed for $U < U_n$, evident on a logarithmic scale with $A = 2.2 \times 10^{-5}$ at $U = 0.28$ and $A = 4.0 \times 10^{-5}$ at $U = 0.3$. Similarly, with $\chi = 0.5$, the amplitude continuously rises for $U < U_c$.

5.2. The mechanism of hysteresis

To elucidate the model's behaviour (4.1), we analyse the energy balance between the work done by the fluid forcing term, $\text{sgn}(\dot{Y})U|Y|$, and the dissipation term, $2\zeta\dot{Y}$, over one oscillation cycle. The fluid forcing energy supplied per cycle is given by

$$E_{in} = \int_{-A}^A U|Y| dY + \int_A^{-A} -U|Y| dY = 2UA^2, \quad (5.1)$$

where the negative sign in the second integrand arises because $\text{sgn}(\dot{Y}) = -1$. The energy dissipated by damping lacks a general analytical form due to the unknown non-harmonic shape of Y , discussed further in § 5.4. Nonetheless, for small ζ , approximating Y as harmonic with angular frequency ω , $Y = A \sin(\omega\tau)$, is feasible. The dissipated energy,

calculated from the damping force and velocity product over a period, is

$$E_d = \int_0^{2\pi/\omega} 2\zeta \dot{Y} \dot{Y} d\tau = 2\pi \zeta \omega A^2. \quad (5.2)$$

These energy expressions are scaled by $m\omega_0^2$, where m is the dimensional mass.

Both E_{in} and E_d scale with A^2 . However, E_{in} remains frequency-independent, whereas E_d is proportional to frequency. This distinction clarifies the oscillator's stable points. The frequency can be approximated by the natural frequency of the left-hand side of the ODE, considering $A \ll Y_{ref}$ (first scenario) or $A \gg Y_{ref}$ (second scenario). In the first scenario, oscillation is damped with a constant augmented stiffness of $1 + \chi$, having a non-damped natural frequency of $\sqrt{1 + \chi}$. Utilizing the ratio between damped and non-damped natural frequencies, $\sqrt{1 - \zeta^2}$ (Fowles 1986), the frequency becomes

$$\omega = \sqrt{(1 + \chi)(1 - \zeta^2)}. \quad (5.3)$$

In the second scenario, the notch term is negligible as it influences only a minor portion of the cycle (see figure 14 for $U > U_c$), and a standard result for the Duffing equation (Jordan & Smith 2007) can be repurposed to obtain the natural frequency as

$$\omega = \sqrt{1 - \frac{3}{4}\gamma A^2}. \quad (5.4)$$

Here, the damping term is neglected.

The critical onset speed, U_c , can be deduced by balancing the energies, $E_d = E_{in}$ ((5.1), (5.2)), along with the small-amplitude frequency formula for ω (5.3):

$$U_c = \pi \zeta \sqrt{(1 + \chi)(1 - \zeta^2)}. \quad (5.5)$$

For $U < U_c$, $E_{in} - E_d$ remains negative, leading to damping of oscillations in absence of harmonic excitation, $\lim_{\tau \rightarrow \infty} A = 0$. As ζ increases, this U_c estimate deviates from numerical results due to overlooked departure from harmonic motion caused by damping-fluid forcing interaction (explained in § 5.4). On the other hand, for $U > U_c$, energy accumulates in the oscillator, resulting in large-amplitude oscillations reaching a limit cycle. The LCO amplitude can be estimated using these equations, employing the large-amplitude frequency approximation (5.4) in the energy balance, $E_d = E_{in}$ ((5.1), (5.2)):

$$A = \sqrt{-\frac{4}{3\gamma} \left(\left(\frac{U}{\pi \zeta} \right)^2 - 1 \right)}. \quad (5.6)$$

The ODE model suggests amplitudes can become very large if U is sufficiently high, although in reality, the system's amplitude is limited by the flag's length and decreases beyond a particular speed, as depicted in figures 5 and 8 or in Eloy *et al.* (2012).

For $\chi > 0$, the transition from large to small A as U decreases below U_d cannot be explained by straightforward analytical expressions due to the interplay between the notch term and the γ -term, preventing estimations of ω and E_d . As A approaches Y_{ref} , the stiff region of the notch that accelerates the motion becomes more important, which causes an additional energy loss, which at U_d leads to the transition to smaller A . Equation (5.5) with $\chi = 0$, representing the critical speed of the notchless oscillator, can be used to approximate U_d .

To demonstrate the mechanism of bistability and hysteresis, figure 15 displays the reference configuration's amplitude and frequency during a velocity sweep (figure 15a_{1,2})

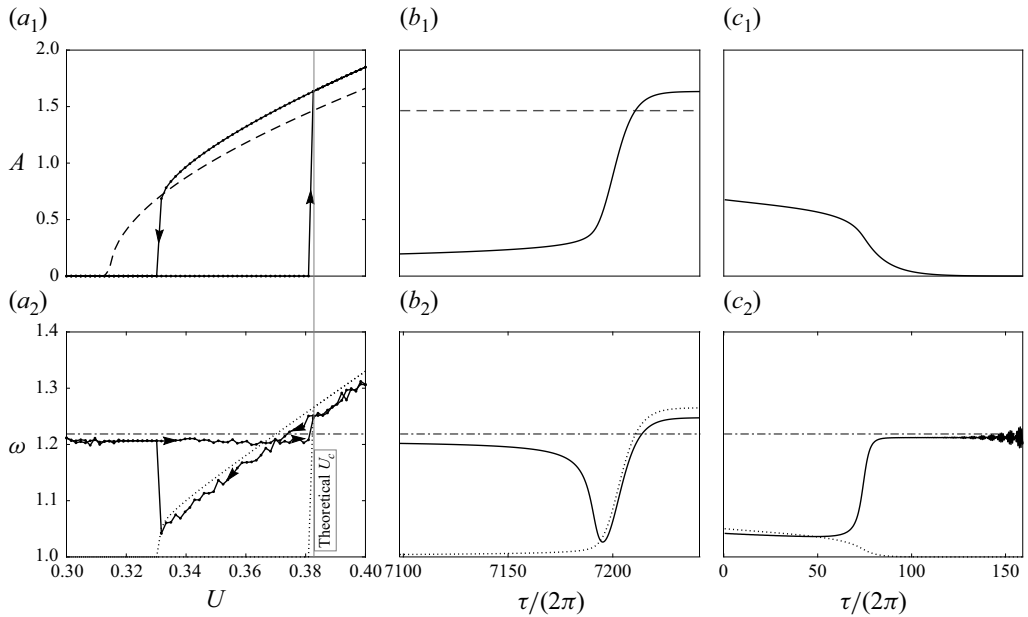


Figure 15. Illustration of the mechanism of bistability and hysteresis. Amplitude A ($a_1 - c_1$) and frequency ω ($a_2 - c_2$, from fast Fourier transform) as a function of velocity U from a stepwise velocity sweep (a_1, a_2); as a function of time $\tau/(2\pi)$ from onset transition (b_1, b_2) and from stop transition (c_1, c_2). Solid lines with dots, numerical model; dashed lines, (5.6); dash-dotted lines, (5.3); dotted lines, (5.4) based on numerical amplitude. Theoretical onset velocity U_c , (5.5).

and transitions between states (figure 15 $b_{1,2}, c_{1,2}$). The analytical expressions (5.3) to (5.6) align fairly with numerical results. As indicated in figure 15 a_1), (5.6) slightly underestimates A , due to the harmonic approximation overestimating energy loss, leading to a power equilibrium at lower amplitudes than the numerical model. While sweeping up from rest with $U < U_c$, the frequency and dissipation rate remain constant (figure 15 $a_{1,2}$) and so high that amplitude growth is inhibited. At U_c , amplitude increases as the fluid forcing provides excess energy, initiating flutter. During this transition (figure 15 $b_{1,2}$), frequency briefly drops while the amplitude rises sharply, then stabilizes; from here, frequency keeps growing with U . During downsweep, the frequency drops below that of small vibrations (possible because $A \gg Y_{ref}$), enabling sustained flutter. Eventually, the frequency returns to its initial value when flutter ends. During this stop transition (figure 15 $c_{1,2}$), oscillations undergo several low-frequency cycles before a frequency increase, influenced by the notch term, causes a rapid amplitude drop, ending the transition.

The experimental data sets that allow for a frequency measurement just prior to flutter typically show an increase in frequency at onset, resembling the model's behaviour, though occasionally a slight decrease is noted. When frequency can be measured over most of the lower hysteresis branch, it generally rises with U (as opposed to being constant in the model). During downsweep, the frequency does not usually drop below the vibration frequency, except in four data sets (CP1, TE2, TP1, TP2) where it does not monotonically rise with U . This represents a subtle distinction between the model and the physical system. The amplitude evolution during onset transition matches results from more complex numerical models (see figure 3a of Michelin *et al.* (2008) and figure 7 of Accardo *et al.* (2013)). As U approaches the critical speed, steady state is reached more

slowly, as noted by Tang & Paidoussis (2007) for their model. Fluctuations in ω in figure 15(c₂) for $100 < \tau/(2\pi)$ are artefacts resulting from computing ω from zero crossings in presence of the excitation frequency ω_e (refer to figure 14c). The fluctuations in ω seen in figure 15(a₂) are due to the limited frequency resolution of the fast Fourier transform in combination with a simple peak-finding method.

To summarize, the bistability for $U_d < U < U_c$ stems from the relative importance of the notch term within the instantaneous range $[-A, A]$. On the lower hysteresis branch, where A is small, the notch enhances stiffness across the period, increasing frequency and damping, which stabilizes the vibration. On the upper branch, where A is large, primarily the hardening spring term $-\gamma Y^2$ influences frequency and hence the damping, while the notch's effect on damping is insufficient to capture the oscillator. Interestingly, the notch does not directly cause bistability by stiffening but rather through enhanced damping. This indirect damping might also affect the physical flag by inducing an energy loss that inhibits flutter onset. However, our data does not show that frequency is lower on the upper branch or that otherwise alike samples with larger flatness defects vibrate at higher frequencies before onset, implying energy loss must have a different origin. Possibly, it may result from material or aerodynamic damping while the flag vibrates differently than its flutter mode, as noted in §3.1. Similarly, the hardening term limits amplitude not by opposing motion directly but through frequency increases and hence dissipation that comes with hardening. This could happen in a fluttering flag, where increase in frequency and in strength of vortex shedding causes energy loss.

5.3. The effects of parameter variations

We explore the effects of parameter variations in figure 16, where critical speeds are plotted as a function of pairs of two parameters. Data points from the reference configuration are identified for orientation. In figure 16(a), the variation of the height of the stiffening notch, χ , is investigated for three damping ratios, ζ . As indicated in (5.5), U_c increases with increasing χ or ζ and decreases inversely. In contrast, U_d remains consistent across χ variations, whereas ζ influences it in approximately proportional amounts to U_c . When $\chi = 0$, $U_c = U_d$, showing no hysteresis. The influence of χ aligns with the experimental finding that stiffening a flag's straight state via flatness defects raises U_c , but negligibly affects U_d (figures 7 and 9; see also Eloy *et al.* (2012)). The rise in critical speeds with higher ζ mirrors the U_c increase seen when the Reynolds number drops in stability studies and numerical models (Connell & Yue 2007), as kinetic energy dissipation pushes an oscillating system towards a static state.

In figure 16(b), the notch half-width Y_{ref} is varied across different hardening coefficients γ . At low $|\gamma|$, U_c remains constant regardless of notch width alterations, but for larger $|\gamma|$, U_c increases as Y_{ref} is increased. Meanwhile, U_d increases consistently with increasing Y_{ref} , and this is more pronounced with higher $|\gamma|$. Large values for both parameters lead to the complete disappearance of hysteresis. These phenomena are explained by the shape of the stiffness term $1 + \chi N(\alpha, \beta, Y/Y_{ref}) - \gamma Y^2$. At lower Y_{ref} , the notch is much narrower than the valley formed by the hardening spring term, bounded vertically by $1 + \chi$ (light grey curve in figure 17a; see figure 13b for labels). The notch width notably affects frequency only at small amplitudes, lightly influencing medium-amplitude oscillations just above U_d , thereby altering U_d itself. In contrast, when the width of the notch approaches that of the valley, the notch blends in with the valley, losing its distinct peak (black curve in figure 17a). Depending on the shoulder slope from α , the notch's top mirrors the underlying parabola $-\gamma Y^2$, forming two local extrema that exceed $1 + \chi$ (medium grey curve in figure 17a). The more the notch blends in and loses its peak,

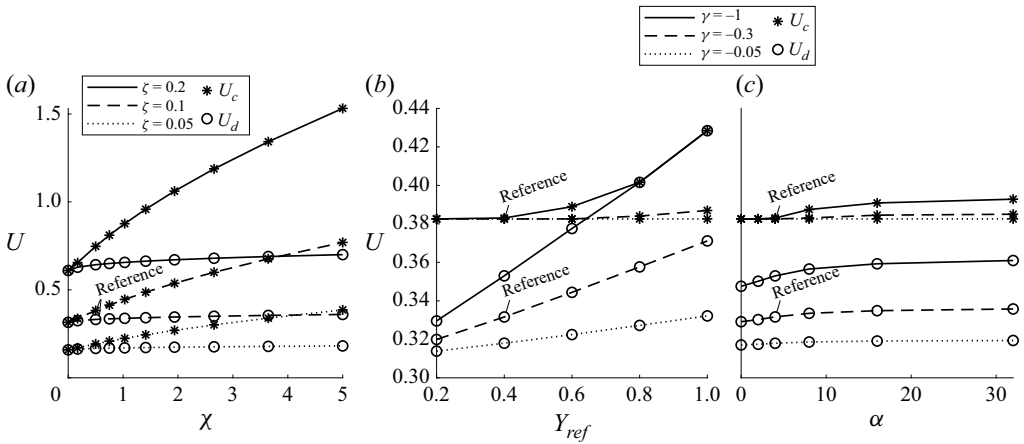


Figure 16. Onset speed, U_c , and stop speed, U_d , as a function of (a) notch height, χ , for multiple damping ratios, ζ , (b) notch half-width, Y_{ref} , for multiple values of the quadratic stiffening coefficient, γ , (c) notch shape parameter, α , for multiple γ . Based on the reference configuration defined in § 4. Here U is flow speed.

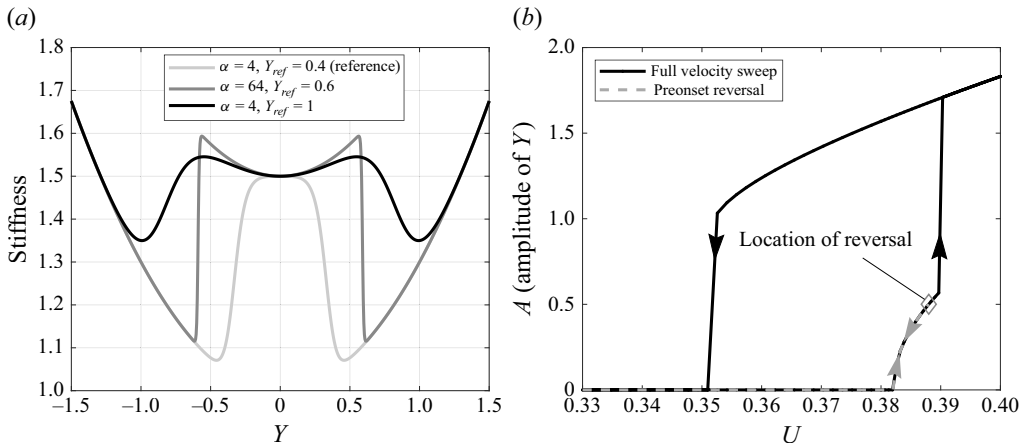


Figure 17. Effects of large notch half-width, Y_{ref} , and/or large notch shape parameter, α . (a) Stiffness term of (4.1) for three parameter sets. (b) Limit cycle amplitude of a velocity sweep with $\alpha = 64$ and $Y_{ref} = 0.6$ whereby U reverses once before large-scale motion sets on, and once after. Here Y is oscillator position, A is the amplitude of Y , U is flow speed. Refer to § 4 for definitions.

the more the effects on onset and stop become indistinguishable, eventually eliminating hysteresis. The extent to which these mechanisms occur in physical flag flutter remains uncertain; for instance, Y_{ref} might relate to the wavenumber of transverse curvature defects in a flag.

In figure 16(c), the notch shape parameter α is modified for different γ values. Changes in γ mainly impact U_d while U_c remains unaffected, as γ is absent from (5.5). However, U_c can be influenced if α is large enough, leading to two peaks in the stiffness term, which increase the onset speed. Here, the amplitude grows to macroscopic levels of the order of Y_{ref} as the oscillator traverses the dimple at the top of the notch (see figure 17b) before transitioning to large-amplitude motion. Lowering U prior to this transition avoids hysteresis (dashed line). This is analogous to wind tunnel findings, where two flutter

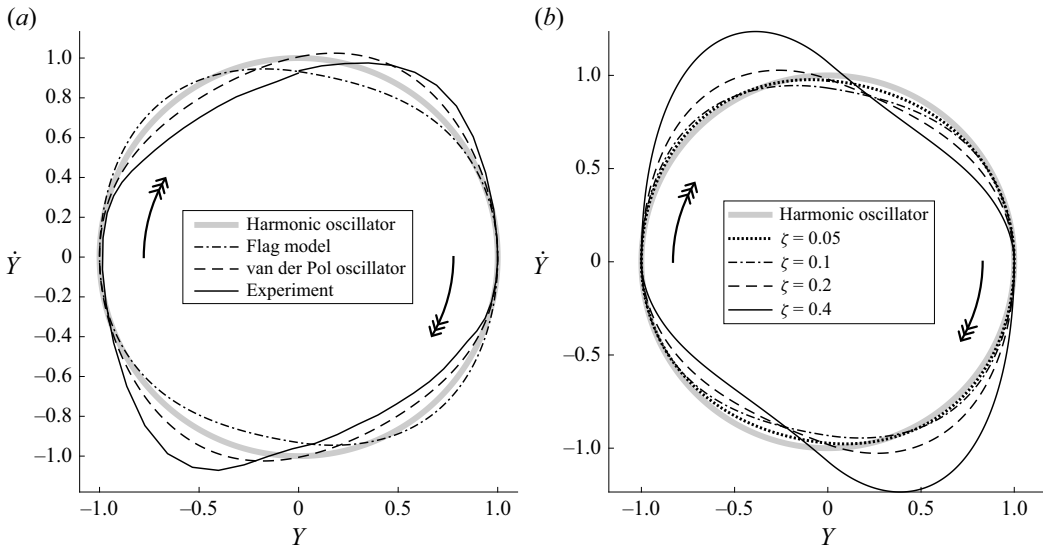


Figure 18. Phase portraits of (a) the ODE model (reference configuration of § 4, flow speed $U = 0.4$), a van der Pol oscillator (nonlinear damping parameter $\varepsilon = 0.2$), and copy paper sample CP3 (refer to table 1) at a flow speed slightly beyond the critical speed ($U = 6.61 \text{ m s}^{-1}$, reduced airspeed $U^* = 19.3$), (b) the ODE model with different amounts of damping, ζ , at a flow speed slightly beyond the critical speed (notch height $\chi = 0$, quadratic stiffening coefficient $\gamma = -0.3$, excitation amplitude $E = 0$). The circular path of harmonic oscillation is given for reference. For normalization, the Y -amplitude was divided by the peak amplitude, A , and the velocity, \dot{Y} , was divided by $A\omega$. Here Y is oscillator position, ω angular frequency. Note that progressive time corresponds to clockwise rotation.

states can occur, showing a small-amplitude LCO before (large-amplitude) flutter onset, as observed in stencil sheet samples (e.g. SS1 in figure 5) and in the plate flutter case of Tang *et al.* (2003).

5.4. Oscillation dynamics

Following our prior analysis focused on amplitudes and frequencies, we conclude this section by contrasting the ODE model's motion, characterized in terms of displacement, Y , and velocity, \dot{Y} , with experimental data and other common oscillator models. This complimentary time-domain viewpoint enhances the understanding of the model's behaviour and highlights both its similarities and differences to other oscillators. Figure 18(a) showcases four phase portraits.

- (i) Harmonic motion serving as a baseline, corresponding to a sinusoidal waveform with a circular phase portrait.
- (ii) The ODE model in reference configuration at $U = 0.4$, exhibiting non-harmonic motion due to non-constant stiffness and external forcing (refer to § 5.2).
- (iii) A weakly nonlinear van der Pol oscillator characterized by the equation

$$\ddot{Y} - \varepsilon(1 - Y^2)\dot{Y} + Y = 0. \quad (5.7)$$

Here, damping is contingent upon the state variable Y , switching between energy dissipation and addition for $|Y| > 1$ and $|Y| < 1$, respectively. This oscillator is utilized in VIV wake models (Facchinetti *et al.* 2004). Those models were an

inspiration for our own model, yet this oscillator is not directly applicable to flag flutter due to its self-exciting nature. We use $\varepsilon = 0.2$ to match the experimental phase portrait.

- (iv) The transverse tip displacement during sample CP3's flutter. When other locations along the rear-half of the flag are chosen instead, the shape of the curve is similar and a little more circular at some of them.

In the experimental motion cycle, \dot{Y} peaks after Y crosses zero. The weakly nonlinear van der Pol oscillator behaves qualitatively similar, whereas in the ODE model, peak velocity occurs before Y crosses zero. While both the van der Pol and ODE models act as relaxation oscillators, a notable distinction is that the van der Pol oscillator's energy input peaks when $-1 < Y < 1$, while damping reduces motion for $|Y| > 1$. Conversely, the ODE model receives energy at the reversal point, with constant damping. The fluid forcing term $\text{sgn}(\dot{Y})U|Y|$, if moved to the left-hand side of (4.1), can be interpreted as a spring term, adding UY^2 in potential energy at every sign change in \dot{Y} . Despite these differences, all motions remain close to harmonic, and the motion patterns of the ODE model and the physical flag can still be considered analogous. For future work, the fluid forcing term in the ODE model could be adjusted to better match the experimental phase relationship.

Figure 18(b) depicts how increased damping affects the system. The peak velocity occurs before Y crosses zero, regardless of damping ζ . A higher ζ results in a departure from harmonic motion, with an asymmetry where the initial acceleration is followed by an increasingly slow phase. For large ζ , the motion transitions to a slow, creeping behaviour, with kinetic energy considerably lower than potential energy (note that due to the normalization by $A\omega$, this is not directly apparent in the phase portraits). Thus, with large ζ , the model fails to accurately describe the motion of a fluttering flag.

6. Conclusion

Our experiments have demonstrated that inherent flatness defects in various sheet materials used for flag flutter experiments significantly enhance the flags' cross-sectional stiffness when not fluttering, with the flutter motion diminishing these defects not only at onset speed but also throughout the upper hysteresis branch, down to nearly the stop speed. This flattening is local and transient. Additionally, we observed the emergence of negative Gaussian curvature along the flag's lateral edges during longitudinal bending. This is an exception to the assumption of Eloy *et al.* (2008, 2012) that Gaussian curvature is energetically too costly. The stiffening from flatness defects, described by an augmented second area moment, moderately correlates with the relative width of the velocity range exhibiting bistability, notably in very flat samples that exhibited minimal hysteresis. To enhance this correlation, more advanced plate mechanics beyond our cross-section approach could be beneficial. Additionally, better control of curvature defects in samples would be ideal but is challenging in wind tunnel experiments. From limited data, we noted that flags with longitudinal curvature had relatively low critical onset speeds despite having significant transverse flatness defects. If verified by further research, this finding may offer practical uses for flag flutter.

Our study does not affirm that flatness defects are the sole cause of hysteresis. Finite hysteresis is observed in numerical models featuring nonlinear fluid dynamics representations, often incorporating a wake model. At flow speeds just below flutter onset, low-amplitude motion appears with a low reduced frequency based on tip amplitude, and no discrete vortices are shed. It is plausible that in perfectly flat flags with a low

mass ratio, vortices produced during flutter favour the motion, maintaining the upper hysteresis branch's flutter while the lower branch's still state remains stable in their absence. Confirming this hypothesis requires further research. To eliminate flatness defects in experiments, one approach is using thicker materials that are soft and dense enough to induce flutter within the wind tunnel's speed limits, yet remain self-supporting and very flat in all directions. The literature and our study also suggest that relatively thick and rigid flags (panels) may exhibit amplitude hysteresis with both small and large amplitude flutter LCOs not attributable to flatness defects.

In studying the kinematics of flag flutter, we have observed that the curvature of large portions of a fluttering flag generally aligns to extract energy from the pressure field. Notably, the free end seems to counteract the pressure field near peak deflection, yet may recover considerable energy after reversal of direction. These observations are based on qualitative interpretations of local curvature and velocity rather than measured or computed pressures. Access to quantitative pressure data would enable a more detailed examination of energy transfer, significantly improving the current literature.

The consolidation of experimental observations has led us to develop the first ODE-based model for flag flutter, which captures several aspects of the phenomenon near critical speeds. This model demonstrates that introducing a stiff region near the neutral point induces a hysteretic response, potentially more marked than in current numerical models, aligning with experimental data. Associated features are discrete state transitions and a growth of both amplitude and frequency with flow speed. Although engineering applications are not immediately foreseen, this model advances our comprehension of flag flutter physics. Contrary to previous assumptions, it is the rise in damping at higher frequencies, rather than the restoring force, that limits oscillation growth. Whether this model observation fully applies to actual systems remains unclear. The model could be enhanced to more accurately reflect flag oscillation dynamics, account for wake effects explicitly, or address amplitude variations at high velocities. Constructing a similar model for the inverted flag appears possible, necessitating a vortex shedding component (Shoele & Mittal 2016).

Supplementary material and movies. Supplementary material and movies are available at <https://doi.org/10.1017/jfm.2025.10692>.

Acknowledgements. The authors acknowledge the assistance from members of the Applied Fluids Research Group and Mr A. Weldon in the Department of Aerospace Engineering at Auburn University, and the staff of the Makerspace of the College of Engineering.

Funding. This research was supported by National Science Foundation (NSF) Award Number CBET – 2145189, monitored by Dr R. Joslin.

Declaration of interests. The authors report no conflict of interest.

Data availability. Data will be made available on request.

Appendix A. Additional details of experimental methods and instrumentation

A.1. Details of clamping conditions

The straightness of the sample holder was assessed through imaging with the edge tracking camera (detailed in § 2.3), repositioned and recalibrated at a reduced aperture for a large depth of field. Spacers simulated the presence of flag samples of different thicknesses. The maximum deviation from a best fit line through six or seven manually selected points was used to quantify straightness. The median of this quantity over five repetitions is reported in table 3. Admitting that the image resolution was a little low for this purpose, which

Spacer thickness (μm)	104	211	254
Median of maximum deviation (μm)	43	38	30

Table 3. Assessment of the sample holder's straightness. Median of maximum deviation from a best-fit line for different spacers.

resulted in some scatter from the manual selection, we are confident that the slightly imperfect straightness of the sample holder can hardly have any significant effect on the results. The flatness defects inherent to the samples were mostly much larger than those that may have been introduced by this imperfect straightness.

Ideally, the flag clamping should be absolutely rigid and provide the corresponding reaction forces to the flag. In our experiments, the heavier the flag under test, the greater were the measured reaction forces during flutter. The maximum amplitudes of lateral motion of the flag root as measured by edge tracking were of the order of 0.1 mm for the lightest (copy paper) flags and 0.4 mm for the heaviest (cardstock and stencil sheet). Since we are not aware of any publications that discuss the influence of imperfectly rigid clamping on flag flutter, we have no basis to judge possible effects. Based on the tiny amplitude ratio of these vibrations with respect to the flag dimensions and the tip motion, we assume the vibrations do not matter.

The frequency content of the force signal of all continuous velocity sweeps was visualized as a spectrogram obtained through short-time Fourier transformation. In only two data sets, during quasisteady acceleration before flutter onset, structural vibrations at the motor drive's frequency were observed, likely from an excitation of the flag. The associated data points are marked in the figures of this paper. In none of the data sets, however, the frequency of the fluttering flag coincided with the motor drive's frequency at any time.

A.2. Details of stereo motion tracking and uncertainty

One side of the calibration plate for stereo motion tracking had a coarse chequerboard pattern with 12.7 mm pitch for calibration, whereas the other side had a finer pattern with 4.064 mm pitch for a characterization of the stereo-based shape reconstruction method. This calibration plate was measured on a milling machine by means of a dial indicator with 2.5 μm precision, and the deviations of the measurement points from a best-fit plane were below 8 μm (root mean square (r.m.s.) 4 μm) on the calibration side and 9 μm (r.m.s. 5 μm) on the characterization side.

For each calibration, between 20 and 33 image pairs of the characterization side were reconstructed, which resulted in the following statistics. The highest deviation from the best-fit plane had a median between 85 μm and 135 μm , the 90 % percentile of deviation was globally below 50 μm and the median r.m.s. deviation was globally below 33 μm . The largest deviations were always localized at the corners of the flag, possibly due to aberrations from the pinhole camera model in those regions of the images. This indicates that the motion tracking method can resolve flatness defects of the order of the thickness of a sheet of copy paper, which is nominally 100 μm . When the relative cross-sectional stiffness, I/I_{flat} (defined in § 2.3), was evaluated from these images assuming the thickness of copy paper, it remained below 1.5 for the majority of the length and never exceeded 2.1. The measurement uncertainty in this quantity drops with the square of the sample thickness, which means it improves with samples thicker than copy paper.

When the magnitude of curvature was evaluated from the images of the characterization side of the plate, which ideally should be zero, the 99 % percentile of it turned out to be of the order of $0.3 \pm 0.05 \text{ rad m}^{-1}$ where smoothing splines plus Gaussian smoothing on the computed curvatures were used (as in [figure 11](#)), and $2 \pm 0.6 \text{ rad m}^{-1}$ where derivatives were evaluated directly (as in Supplementary movies [5–7](#)).

Appendix B. Numerical implementation

The model is solved as a system of first-order ODEs with MATLAB's standard ODE solver `ode15s`. This solver features adaptive time stepping through the definition of absolute and relative convergence tolerances, `AbsTol` and `RelTol`, which we utilize to establish time step convergence. As a test case, we use the reference configuration and observe the transition from zero initial conditions to flutter at a speed slightly above the onset speed. As convergence metrics, we chose the final amplitude, the final frequency, and the time it takes to reach 80 % of the final amplitude. The time-based metric is the most sensitive to the convergence criteria; it levels out for $\text{AbsTol} \leq 10^{-8}$ in combination with $\text{RelTol} \leq 10^{-7}$. The smaller E is chosen, the smaller `AbsTol` must be to reach convergence. The data presented in this paper were obtained with $10^{-10} \leq \text{AbsTol} \leq 10^{-8}$ and $\text{RelTol} = 10^{-7}$.

To simulate a wind tunnel experiment where the airspeed is increased stepwise from zero and then decreased stepwise to zero, the calculation starts with zero initial conditions, $Y = \dot{Y} = 0$, and $U = 0$. The ODE is integrated until either an LCO is detected or a certain timeout in terms of τ is reached, whichever occurs earlier. With the terminal system state in terms of Y and \dot{Y} as new initial condition, and the next value for U , the calculation is restarted. This process is repeated for all U of interest. The LCO detection is based on the correlation of two consecutive segments of the solution and executed at regular intervals in the solution process.

To obtain the onset and stop speeds for a given set of parameters, two bisection searches are performed. To find the onset speed, the calculation is always initialized with the terminal state of the execution at the highest U that did not lead to flutter, or, if that is unavailable, with $Y = \dot{Y} = 0$. Once the onset speed is determined, the stop speed is found through bisection where the calculation starts with the terminal state of the execution at the lowest U that still produced sustained flutter. For the purpose of the bisection search, flutter is defined as the oscillator reaching an LCO amplitude greater than Y_{ref} , even in the case that $\chi = 0$. The initial search window is $U \in [0, 2]$ or $U \in [0, 4]$ and the number of iterations for bisection is 12 or 13, so that the critical speeds are determined up to an uncertainty of at most $\pm 2^{-12} = \pm 2.4 \times 10^{-4}$.

As a metric of independence of the parameters E and ω_e , we use the width of the hysteresis loop, $\mathcal{E} \equiv (U_c - U_d)/U_d$. With the reference configuration as a baseline, the variation of \mathcal{E} with E and ω_e shows a plateau for $E \leq 10^{-4}$ and $\omega_e \leq 0.3$. We chose $E = 10^{-5}$ and $\omega_e = 0.1$ for this paper.

REFERENCES

- ACCARDO, G., EUGENI, M., MASTRODDI, F. & ROMANO, G. 2013 Experimental and numerical modelling for flag flutter. In *Proceedings of the XXII National Conference of the Italian Association of Aeronautics and Astronautics*, pp. 1–16.
- ALBEN, S. 2015 Flag flutter in inviscid channel flow. *Phys. Fluids* **27** (3), 033603.
- ALBEN, S. 2022 Dynamics of flags over wide ranges of mass and bending stiffness. *Phys. Rev. Fluids* **7** (1), 013903.
- ALBEN, S. & SHELLEY, M.J. 2008 Flapping states of a flag in an inviscid fluid: bistability and the transition to chaos. *Phys. Rev. Lett.* **100** (7), 074301.

- ALLEN, J. J. & SMITS, A. J. 2001 Energy harvesting eel. *J. Fluid. Struct.* **15** (3-4), 629–640.
- AVELAR, A.H.DE F., STÓFEL, M.A.G.E., CANESTRI, J.A. & HUEBNER, R. 2017 Analytical approach on leaflet flutter on biological prosthetic heart valves. *J. Braz. Soc. Mech. Sci.* **39**, 4849–4858.
- CONNELL, B.S.H. & YUE, D.K.P. 2007 Flapping dynamics of a flag in a uniform stream. *J. Fluid Mech.* **581**, 33–67.
- DOU, Z., RIPS, A., JACOB, L. & MITTAL, R. 2020 Experimental characterization of the flow-induced flutter of a suspended elastic membrane. *AIAA J.* **58** (1), 445–454.
- ELOY, C., KOFMAN, N. & SCHOUVEILER, L. 2012 The origin of hysteresis in the flag instability. *J. Fluid Mech.* **691**, 583–593.
- ELOY, C., LAGRANGE, R., SOUILLIEZ, C. & SCHOUVEILER, L. 2008 Aeroelastic instability of cantilevered flexible plates in uniform flow. *J. Fluid Mech.* **611**, 97–106.
- FACCHINETTI, M.L., DE LANGRE, E. & BLOLEY, F. 2004 Coupling of structure and wake oscillators in vortex-induced vibrations. *J. Fluid. Struct.* **19** (2), 123–140.
- FOWLES, G.R. 1986 *Analytical Mechanics*. 4th edn. CBS College Publishing.
- GALLEGOS, R.K.B. & SHARMA, R.N. 2017 Flags as vortex generators for heat transfer enhancement: gaps and challenges. *Renew. Sustain. Energy Rev.* **76**, 950–962.
- GIACOMELLO, A. & PORFIRI, M. 2011 Underwater energy harvesting from a heavy flag hosting ionic polymer metal composites. *J. Appl. Phys.* **109** (8), 084903.
- GIBBS, S. C., FICHERA, S., ZANOTTI, A., RICCI, S. & DOWELL, E.H. 2014 Flow field around the flapping flag. *J. Fluid. Struct.* **48**, 507–513.
- HAN, S.M., BENAROYA, H. & WEI, T. 1999 Dynamics of transversely vibrating beams using four engineering theories. *J. Sound Vib.* **225** (5), 935–988.
- HIROAKI, K. & WATANABE, M. 2024 Flutter generated on a sheet in 3d flow: influence of aspect ratio of sheets on post-critical and hysteretic behavior. *Nonlinear Dyn.* **112** (18), 15757–15770.
- HOWELL, R. M., LUCEY, A. D., CARPENTER, P. W. & PITMAN, M. W. 2009 Interaction between a cantilevered-free flexible plate and ideal flow. *J. Fluid. Struct.* **25** (3), 544–566.
- HUANG, L. 1995 Flutter of cantilevered plates in axial flow. *J. Fluid. Struct.* **9** (2), 127–147.
- JIA, Y., JIA, L., SU, Z. & YUAN, H. 2018 Experimental investigation of flow field around the elastic flag flapping in periodic state. *Mod. Phys. Lett. B* **32** (12–13), 1840031.
- JOHNSON, E.L., WU, M.C.H., XU, F., WIESE, N.M., RAJANNA, M.R., HERREMA, A.J., GANAPATHYSUBRAMANIAN, B., HUGHES, T.J.R., SACKS, M.S. & HSU, M.-C. 2020 Thinner biological tissues induce leaflet flutter in aortic heart valve replacements. *Proc. Natl Acad. Sci.* **117** (32), 19007–19016.
- JORDAN, D. & SMITH, P. 2007 *Nonlinear Ordinary Differential Equations: an Introduction for Scientists and Engineers*. OUP Oxford.
- KIM, S., HUANG, W.-X. & SUNG, H.J. 2010 Constructive and destructive interaction modes between two tandem flexible flags in viscous flow. *J. Fluid Mech.* **661**, 511–521.
- LANGTHJEM, M.A. 2019 On the mechanism of flutter of a flag. *Acta Mech.* **230**, 3759–3781.
- LEE, J.B., PARK, S.G., KIM, B., RYU, J. & SUNG, H.J. 2017 Heat transfer enhancement by flexible flags clamped vertically in a Poiseuille channel flow. *Int. J. Heat Mass Tran.* **107**, 391–402.
- LIU, H., ZHANG, S., KATHIRESAN, R., KOBAYASHI, T. & LEE, C. 2012 Development of piezoelectric microcantilever flow sensor with wind-driven energy harvesting capability. *Appl. Phys. Lett.* **100** (22), 223905.
- MARTIN, A. 2006 Experimental study of drag from a fluttering flag, Master’s thesis. Oklahoma State University.
- MAVROYIAKOUMOU, C. & ALBEN, S. 2022 Membrane flutter in three-dimensional inviscid flow. *J. Fluid Mech.* **953**, A32.
- MICHELIN, S. & DOARÉ, O. 2013 Energy harvesting efficiency of piezoelectric flags in axial flows. *J. Fluid Mech.* **714**, 489–504.
- MICHELIN, S., SMITH, S.G.L. & GLOVER, B.J. 2008 Vortex shedding model of a flapping flag. *J. Fluid Mech.* **617**, 1–10.
- MORETTI, P.M. 2004 Flag flutter amplitudes. *Flow Induced Vibrations, Paris*, pp. 6–9.
- MÜLLER, U.K. 2003 Fish’n flag. *Science* **302** (5650), 1511–1512.
- ÖZKAN, M., ERKAN, O. & BASARAN, S. 2024 Flag fluttering-triggered piezoelectric energy harvester at low wind speed conditions. *Energy Technol-GER.* **12** (4), 2301194.
- PINI, V., RUZ, J. J., KOSAKA, P.M., MALVAR, O., CALLEJA, M. & TAMAYO, J. 2016 How two-dimensional bending can extraordinarily stiffen thin sheets. *Sci. Rep-UK.* **6** (1), 29627.
- SHELLEY, M., VANDENBERGHE, N. & ZHANG, J. 2005 Heavy flags undergo spontaneous oscillations in flowing water. *Phys. Rev. Lett.* **94** (9), 094302.

- SHELLEY, M.J. & ZHANG, J. 2011 Flapping and bending bodies interacting with fluid flows. *Annu. Rev. Fluid Mech.* **43** (1), 449–465.
- SHOELE, K. & MITTAL, R. 2014 Computational study of flow-induced vibration of a reed in a channel and effect on convective heat transfer. *Phys. Fluids* **26** (12), 127103.
- SHOELE, K. & MITTAL, R. 2016 Energy harvesting by flow-induced flutter in a simple model of an inverted piezoelectric flag. *J. Fluid Mech.* **790**, 582–606.
- TANEDA, S. 1968 Waving motions of flags. *J. Phys. Soc. Japan* **24** (2), 392–401.
- TANG, D.M., YAMAMOTO, H. & DOWELL, E. H. 2003 Flutter and limit cycle oscillations of two-dimensional panels in three-dimensional axial flow. *J. Fluid. Struct.* **17** (2), 225–242.
- TANG, L. & PAÏDOUSSIS, M.P. 2007 On the instability and the post-critical behaviour of two-dimensional cantilevered flexible plates in axial flow. *J. Sound Vib.* **305** (1–2), 97–115.
- THOMA, D. 1939 Warum flattert die fahne. *Mitteilungen des Hydraulischen Instituts der Technischen Hochschule München* **9**, 30–34.
- TIAN, F.-B. 2013 Role of mass on the stability of flag/flags in uniform flow. *Appl. Phys. Lett.* **103** (3), 034101.
- VIROT, E., AMANDOLESE, X. & HÉMON, P. 2013 Fluttering flags: an experimental study of fluid forces. *J. Fluid. Struct.* **43**, 385–401.
- WATANABE, Y., SUZUKI, S., SUGIHARA, M. & SUEOKA, Y. 2002 An experimental study of paper flutter. *J. Fluid. Struct.* **16** (4), 529–542.
- YU, Y., LIU, Y. & AMANDOLESE, X. 2019 A review on fluid-induced flag vibrations. *Appl. Mech. Rev.* **71** (1), 010801.
- ZHU, L. & PESKIN, C.S. 2002 Simulation of a flapping flexible filament in a flowing soap film by the immersed boundary method. *J. Comput. Phys.* **179** (2), 452–468.